

See discussions, stats, and author profiles for this publication at:
<https://www.researchgate.net/publication/261983436>

DETERMINATION METHODS OF DENSITIES AND ENERGY LEVELS OF IMPURITIES AND DEFECTS AFFECTING...

Chapter · January 2011

CITATIONS

0

READS

29

1 author:



Hideharu Matsuura

Osaka Electro-Communication University

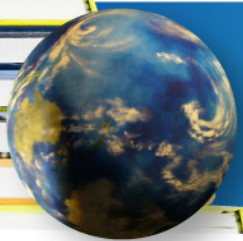
101 PUBLICATIONS 1,355 CITATIONS

SEE PROFILE

Some of the authors of this publication are also working on these related projects:



Radiation Damage in Semiconductors [View project](#)



NOVA

SCIENCE PUBLISHERS, INC.

DETERMINATION METHODS OF DENSITIES AND
ENERGY LEVELS OF IMPURITIES AND DEFECTS
AFFECTING MAJORITY-CARRIER
CONCENTRATION IN NEXT-GENERATION
SEMICONDUCTORS

Hideharu Matsuura

400 Oser Avenue, Suite 1600
Hauppauge, N. Y. 11788-3619
Phone (631) 231-7269
Fax (631) 231-8175
E-mail: main@novapublishers.com
<http://www.novapublishers.com>

In: "Advances in Condensed Matter
and Materials Research, Volume 10"

Editors: H. Geelvinck and S. Reynst

ISBN: 978-1-61209-533-2 2011

The exclusive license for this PDF is limited to personal website use only. No part of this digital document may be reproduced, stored in a retrieval system or transmitted commercially in any form or by any means. The publisher has taken reasonable care in the preparation of this digital document, but makes no expressed or implied warranty of any kind and assumes no responsibility for any errors or omissions. No liability is assumed for incidental or consequential damages in connection with or arising out of information contained herein. This digital document is sold with the clear understanding that the publisher is not engaged in rendering legal, medical or any other professional services.

Chapter 7

DETERMINATION METHODS OF DENSITIES AND ENERGY LEVELS OF IMPURITIES AND DEFECTS AFFECTING MAJORITY-CARRIER CONCENTRATION IN NEXT-GENERATION SEMICONDUCTORS

*Hideharu Matsuura**

Osaka Electro-Communication University, Japan

Abstract

Wide bandgap semiconductors such as SiC, GaN, and diamond have a potential for use in high power and high frequency devices, while narrow bandgap semiconductors such as the GaSb family have a potential for near- and mid-infrared laser diodes and photo-detectors for detecting CO₂, CH₄, NO_x, and SO_x. In these next-generation semiconductors, it is essential to precisely determine the densities and energy levels of dopants (donors or acceptors) as well as unintentionally-introduced impurities and defects, which affect the majority-carrier concentrations in semiconductors.

We have developed a graphical peak analysis method called Free Carrier Concentration Spectroscopy (FCCS), which can accurately determine them using the temperature dependence of the majority-carrier concentration without any assumptions regarding dopant species, impurities, and defects. We have determined the densities and energy levels in undoped, N-doped or Al-doped SiC. Moreover, the dependence of the energy level of each dopant species on dopant density has been obtained. From the temperature dependence of the majority-carrier concentration in SiC irradiated by high-energy electrons, the dependence of the density of each dopant or defect on fluence has been determined.

Because wide bandgap semiconductors have a low dielectric constant and a hole effective mass heavier than an electron effective mass, the energy levels of acceptor species are expected to be deep. When x is larger, on the other hand, the donor level of Te in Al _{x} Ga_{1- x} Sb is changed from shallow to deep, just like Al _{x} Ga_{1- x} As. In these semiconductors, the density of dopants determined from the temperature dependence of the majority-carrier concentration is much higher than the concentration of dopant

*E-mail address: matsuura@isc.osakac.ac.jp

species determined by secondary ion mass spectroscopy. When the energy level of dopant species is deep, the excited states of the dopant should affect the majority-carrier concentration. Therefore, we have introduced the occupation function of the dopant with deep energy level, which includes the influence of its excited states, instead of the Fermi-Dirac distribution function. Using the occupation function we have proposed, we have investigated semiconductors with deep level dopants by FCCS using the temperature dependence of the majority-carrier concentration.

Recently, high-resistivity or semi-insulating semiconductors have been required to use as substrates of GaN field-effect transistors and as active layers of X-ray detectors capable of operating at room temperature. Because these defects affect the majority-carrier concentrations in high-resistivity or semi-insulating semiconductors and degrade the device performance, it is required to accurately determine the densities and energy levels of defects with deep energy levels. Transient capacitance methods such as Deep Level Transient Spectroscopy cannot apply higher-resistivity semiconductors. Therefore, we have been developing a graphical peak analysis method using an isothermal transient current in the diode, called Discharge Current Transient Spectroscopy (DCTS). Using DCTS, we have determined the densities, emission rates, and energy levels of deep defects in semi-insulating SiC and thin insulators. Moreover, the density-of-states in high-resistivity amorphous semiconductors are investigated.

PACS 71.55.-i, 71.55.Ht, 72.20.Jv, 73.61.Le

Keywords: Determination of densities and energy levels, Next-generation semiconductor, SiC, GaN, Diamond, InGaSb, AlGaSb, Donor, Acceptor, Deep level.

1. Introduction

In this chapter, we discuss methods to evaluate impurities and defects that affect the majority-carrier concentration in a semiconductor whose resistivity varies from low to extremely high.

The densities and energy levels of traps (i.e., impurities or defects) have usually been evaluated using deep level transient spectroscopy (DLTS) [1]. However, a quantitative relationship between the majority-carrier concentration and the trap densities cannot be obtained using DLTS. The reason for this is that in the DLTS analysis, the following approximation is assumed.

$$\begin{aligned} C(t) &= C(\infty) \sqrt{1 - \frac{N_T}{N_{\text{dopant}} + N_T} \exp\left(-\frac{t}{\tau_T}\right)} \\ &\simeq C(\infty) \left[1 - \frac{N_T}{2(N_{\text{dopant}} + N_T)} \exp\left(-\frac{t}{\tau_T}\right) \right] \end{aligned} \quad (1)$$

when

$$\frac{N_T}{N_{\text{dopant}} + N_T} \ll 1, \quad (2)$$

where $C(t)$ is the transient capacitance after removal of the filling pulse and return to the steady-state reverse bias voltage (V_R) in the DLTS measurement sequence, $C(\infty)$ is the steady-state capacitance at V_R , N_{dopant} is the dopant density (i.e., donor or acceptor density), N_T is the trap density, and τ_T is the time constant corresponding to the trap. Based

on Eq. (2), DLTS can determine the density and energy level of the trap only when N_T is much lower than N_{dopant} , indicating that the trap determined by DLTS barely affects the majority-carrier concentration. If the densities and energy levels of traps can be determined using the experimental majority-carrier concentration, the relationship between the majority-carrier concentration and the trap densities can be investigated directly. Therefore, we discuss a unique method to characterize them from the temperature dependence of the majority-carrier concentration obtained by Hall-effect measurements.

Transient capacitance methods such as DLTS, furthermore, cannot be applied to high-resistivity semiconductors, because the measured capacitance of a diode is determined by the thickness of the diode, not by the depletion region of the junction due to its long dielectric relaxation time. For example, the resistivity (ρ) of high-purity SiC is strongly affected by intrinsic defects located in its midgap, which capture the majority carriers. Therefore, it is necessary to investigate the nature of the deep levels in high-purity SiC. To characterize the intrinsic defects in SiC, however, N-doped low-resistivity SiC irradiated by electrons has been intensively investigated by DLTS [2, 3].

Thermally stimulated current (TSC) [4] is suitable for characterizing traps in high-resistivity or semi-insulating semiconductors. The TSC signal, $I_{\text{TSC}}(T)$, is theoretically given by

$$I_{\text{TSC}}(T) = qA \sum_{i=1} N_{\text{Ti}} \nu_{\text{Ti}} \exp \left[-\frac{\Delta E_{\text{Ti}}}{kT} - \frac{\nu_{\text{Ti}}}{\beta} \int_{T_0}^T \exp \left(-\frac{\Delta E_{\text{Ti}}}{kT} \right) dT \right] + I_{\text{ssl}}(T), \quad (3)$$

where q is the electron charge, k is the Boltzmann constant, β is the heating rate, N_{Ti} is the density for an i th trap, ΔE_{Ti} is the activation energy for the i th trap, ν_{Ti} is the attempt-to-escape frequency for the i th trap, T_0 is the temperature at which heating is started, $I_{\text{ssl}}(T)$ is the steady-state leakage current at a measurement temperature (T), and A is the electrode area. It should be noted that Eq. (3) is available only in thermionic emission processes. Parameters for fitting a curve to the experimental $I_{\text{TSC}}(T)$ are the sets of N_{Ti} , ΔE_{Ti} and ν_{Ti} . However, it is difficult to analyze experimental TSC data when traps with close emission rates are included. Moreover, because the effect of pyroelectric currents and the temperature dependence of the steady-state leakage current must be considered in the TSC analysis, an isothermal measurement is more suitable for characterizing traps than TSC is. Therefore, we discuss a unique method to characterize them using isothermal transient current measurements.

2. Temperature Dependence of Majority-Carrier Concentration

The temperature dependence of the majority-carrier concentration has a lot of information on impurities and defects. In n-type semiconductors, for example, the temperature dependence of the electron concentration, $n(T)$, can be expressed as [5]

$$n(T) = \sum_{i=1} N_{\text{Di}} [1 - f_{\text{FD}}(E_{\text{Di}})] - \sum_{j=1} N_{\text{TEj}} f_{\text{FD}}(E_{\text{TEj}}) - N_{\text{A}}, \quad (4)$$

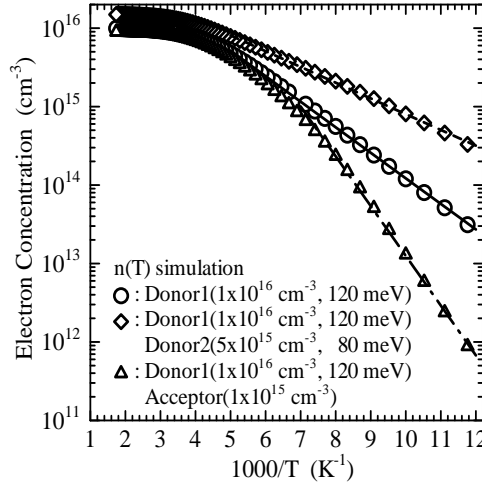


Figure 1. Simulations of temperature-dependent electron concentration for three cases of one donor, two donors, and one donor and one acceptor.

in the temperature range in which a temperature-dependent hole concentration, $p(T)$, is much less than $n(T)$, where N_{Di} and E_{Di} are the density and energy level of an i th donor, N_{TEj} and E_{TEj} are the density and energy level of a j th electron trap that is negative when it captures an electron from the conduction band, N_A is the acceptor density, $f_{FD}(E_{Di})$ and $f_{FD}(E_{TEj})$ are the Fermi-Dirac distribution function for donors and electron traps, given by [5]

$$f_{FD}(E) = \frac{1}{1 + \frac{1}{2} \exp\left(\frac{E - E_F(T)}{kT}\right)}, \quad (5)$$

and $E_F(T)$ is the Fermi level at T . From $n(T)$, therefore, we can determine the densities and energy levels of donors and electron traps.

The temperature dependencies of the majority-carrier concentration and mobility can usually be obtained by Hall-effect measurements. When a sample is an n-type epilayer on a substrate, for example, the substrate should be a p-type or semi-insulating semiconductor.

Let us evaluate donors using the $n(T)$ simulations for 4H-SiC in the cases of one donor (\circ), two donors (\diamond), and one donor and one acceptor (\triangle) in Fig. 1. Here, the density and energy level are $1 \times 10^{16} \text{ cm}^{-3}$ and $E_C - 0.12 \text{ eV}$ for Donor1, and $5 \times 10^{15} \text{ cm}^{-3}$ and $E_C - 0.08 \text{ eV}$ for Donor2, respectively, and the acceptor density is $1 \times 10^{15} \text{ cm}^{-3}$.

In the case of one donor, which is described in university text books, $n(T)$ can be expressed by the following two equations:

$$n(T) = N_D [1 - f_{FD}(E_D)] \quad (6)$$

and

$$n(T) = N_C(T) \exp\left(-\frac{E_C - E_F(T)}{kT}\right), \quad (7)$$

where

$$N_C(T) = N_{C0} k^{3/2} T^{3/2}, \quad (8)$$

$$N_{C0} = 2 \left(\frac{2\pi m_e^*}{h^2} \right)^{3/2} M_C, \quad (9)$$

N_D is the donor density, E_C is the conduction band maximum, m_e^* is the electron effective mass, M_C is the number of equivalent minima in the conduction band, and h is the Planck's constant. At low temperatures where

$$N_D \gg \frac{N_C(T)}{8} \exp \left(-\frac{E_C - E_D}{kT} \right), \quad (10)$$

the following equation is derived using Eqs. (6) and (7).

$$n(T) \cong \sqrt{\frac{N_C(T)N_D}{2}} \exp \left(-\frac{E_C - E_D}{2kT} \right) \quad (11)$$

$$= T^{3/4} \left(\frac{2\pi m_e^* k}{h^2} \right)^{3/4} \sqrt{M_C} \sqrt{N_D} \exp \left(-\frac{E_C - E_D}{2kT} \right). \quad (12)$$

Therefore, the donor level ($E_C - E_D$) is determined from the slope at low temperatures in Fig. 1. Moreover, N_D is equal to the saturation value in Fig. 1.

From each $n(T)$ at low temperatures in Fig. 1, the straight solid, broken and dotted-dashed lines can be drawn for the cases of one donor, two donors, and one donor and one acceptor, respectively. We can obtain the correct results that the density and energy level of the donor are determined to be $1 \times 10^{16} \text{ cm}^{-3}$ and 0.12 eV for \bigcirc , respectively. On the other hand, the density and energy level of the donor are determined to be $1.5 \times 10^{16} \text{ cm}^{-3}$ and 0.08 eV for \diamond , and $0.9 \times 10^{16} \text{ cm}^{-3}$ and 0.25 eV for \triangle , which are incorrect results. Therefore, this analysis can be applied only when we can confirm that the semiconductor includes only one type of donor species.

In the case of one donor and one acceptor, the following equation is derived using Eqs. (6) and (7).

$$\frac{1}{T^{3/2}} \cdot \frac{n(T)[n(T) + N_A]}{(N_D - N_A) - n(T)} = \left(\frac{2\pi m_e^* k}{h^2} \right)^{3/2} M_C \exp \left(-\frac{E_C - E_D}{kT} \right). \quad (13)$$

We define y as

$$y = \frac{1}{T^{3/2}} \cdot \frac{n(T)[n(T) + N_A]}{(N_D - N_A) - n(T)}, \quad (14)$$

and we try to search the values of N_A and $(N_D - N_A)$ that make the relationship between y and $1/T$ straight. From the slope of the straight line, the donor level can be determined using Eq. (13).

In the case of more than two types of donor species, the curve-fitting method is applied. Using

$$n(T) = \sum_{i=1}^n N_{Di} [1 - f_{FD}(E_{Di})] - N_A, \quad (15)$$

and Eq. (7), the $n(T)$ can be simulated. By a least-squares fit of the $n(T)$ simulation to the experimental $n(T)$, the fitting parameters of n sets of N_{Di} and E_{Di} as well as N_A are obtained. Prior to the analysis, the number of donor species and the initial values of the parameters should be assumed. The assumptions, however, strongly affect the final results.

In the differential Hall-effect spectroscopy (DHES) [6, 7],

$$-kT \frac{dn(T)}{d\Delta E_F(T)} = \sum_{i=1}^n N_{Di} \frac{2 \exp\left(\frac{\Delta E_{Di} - \Delta E_F(T)}{kT}\right)}{\left[1 + 2 \exp\left(\frac{\Delta E_{Di} - \Delta E_F(T)}{kT}\right)\right]^2} \times \left[1 + \frac{\Delta E_{Di} - \Delta E_F(T)}{kT} \cdot \frac{\partial(kT)}{\partial \Delta E_F(T)}\right] \quad (16)$$

where $\Delta E_{Di} = E_C - E_{Di}$ and $\Delta E_F(T) = E_C - E_F(T)$. When

$$\frac{\Delta E_{Di} - \Delta E_F(T)}{kT} \cdot \frac{\partial(kT)}{\partial \Delta E_F(T)} \ll 1, \quad (17)$$

Eq. (16) can be rewritten approximately as

$$-kT \frac{dn(T)}{d\Delta E_F(T)} \cong \sum_{i=1}^n N_{Di} \frac{2 \exp\left(\frac{\Delta E_{Di} - \Delta E_F(T)}{kT}\right)}{\left[1 + 2 \exp\left(\frac{\Delta E_{Di} - \Delta E_F(T)}{kT}\right)\right]^2}. \quad (18)$$

When we define y as

$$y = -kT \frac{dn(T)}{d\Delta E_F(T)}, \quad (19)$$

the peak of the $y - \Delta E_F(T)$ characteristics occurs at

$$\Delta E_F(T_{\text{peak}i}) = \Delta E_{Di} + kT_{\text{peak}i} \ln 2. \quad (20)$$

However, the differential of the experimental data results in an increase in the observational errors.

As a consequence, we adopt the following criteria for an evaluation function that can determine the densities and energy levels of donors and electron traps from the experimental $n(T)$;

1. not to require any assumptions regarding donor species and electron traps before analysis,
2. not to differentiate the experimental data,
3. to have a peak value at the temperature corresponding to the energy level of each donor or electron trap,
4. to be able to verify the values determined.

3. Free Carrier Concentration Spectroscopy

3.1. Basic Concept

Transient capacitance methods, such as DLTS [1] and isothermal capacitance transient spectroscopy (ICTS) [8], can uniquely determine the densities and energy levels of traps in semiconductors, because each peak in the signal corresponds one-to-one to a trap. For example, the ICTS signal is defined as $S(t) \equiv t dC(t)^2/dt$. Since $S(t)$ is theoretically described as the sum of $N_{Ti} e_{Ti} t \exp(-e_{Ti} t)$, it has a peak value of $N_{Ti} \exp(-1)$ at a peak time of $t_{peaki} = 1/e_{Ti}$. Here, e_{Ti} is the emission rate of an i th trap. Therefore, the function $N_{Ti} e_{Ti} t \exp(-e_{Ti} t)$ plays an important role in the ICTS analysis.

To analyze the experimental $n(T)$, we introduced the function theoretically described as the sum of $N_{Di} \exp(-\Delta E_{Di}/kT)/kT$ [9, 10]. The function $N_{Di} \exp(-\Delta E_{Di}/kT)/kT$ has a peak at $T_{peaki} = \Delta E_{Di}/k$. If we can introduce a function in which the peak appears at $T_{peaki} = (\Delta E_{Di} - E_{ref})/k$, we can shift the peak temperature to the measurement temperature range by changing the parameter E_{ref} . This indicates that we can determine N_{Di} and ΔE_{Di} in a wide range of donor levels in a limited measurement temperature range. Therefore, the function to be evaluated should be approximately described as the sum of $N_{Di} \exp[-(\Delta E_{Di} - E_{ref})/kT]/kT$. It should be noted that N_{Di} and ΔE_{Di} determined by this method are independent of E_{ref} .

3.2. Theoretical Consideration

3.2.1. n-type Semiconductors

From Eqs. (4) and (7), a favorable function to determine N_{Di} , ΔE_{Di} , N_{TEj} , ΔE_{TEj} and N_A can be defined as

$$H(T, E_{ref}) \equiv \frac{n(T)^2}{(kT)^{5/2}} \exp\left(\frac{E_{ref}}{kT}\right). \quad (21)$$

Substituting Eq. (4) for one of the $n(T)$ in Eq. (21) and substituting Eq. (7) for the other $n(T)$ in Eq. (21) yield

$$\begin{aligned} H(T, E_{ref}) = & \sum_{i=1} \frac{N_{Di}}{kT} \exp\left(-\frac{\Delta E_{Di} - E_{ref}}{kT}\right) I_n(\Delta E_{Di}) \\ & + \sum_{j=1} \frac{N_{TEj}}{kT} \exp\left(-\frac{\Delta E_{TEj} - E_{ref}}{kT}\right) I_n(\Delta E_{TEj}) \\ & - \frac{N_{comp} N_{C0}}{kT} \exp\left(\frac{E_{ref} - \Delta E_F(T)}{kT}\right), \end{aligned} \quad (22)$$

where

$$\Delta E_{TEj} = E_C - E_{TEj}, \quad (23)$$

$$I_n(\Delta E) = \frac{N_{C0}}{2 + \exp\left(\frac{\Delta E_F(T) - \Delta E}{kT}\right)}, \quad (24)$$

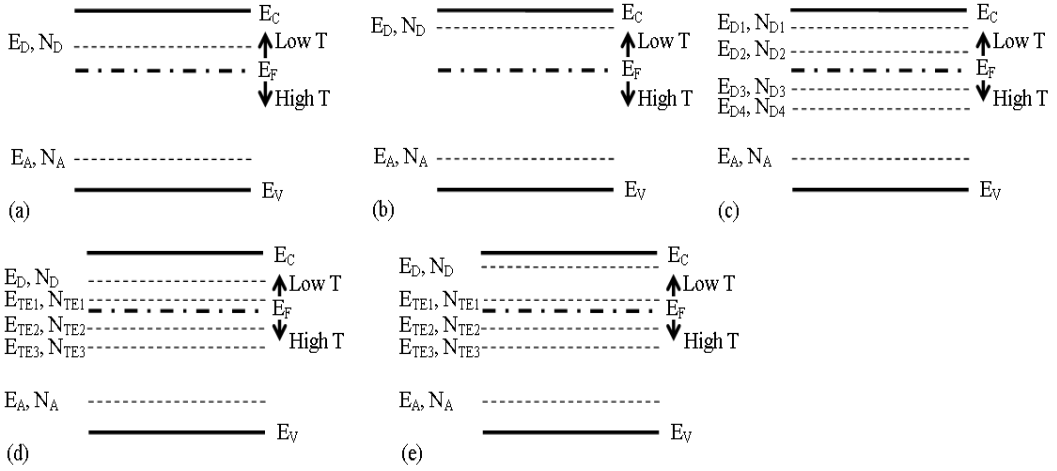


Figure 2. Five cases. The Fermi level moves from LowT to HighT as the measurement temperature rises.

and N_{comp} is the compensating density given by

$$N_{\text{comp}} = N_A + \sum_{j=1} N_{\text{TE}j}. \quad (25)$$

The function

$$\frac{N_i}{kT} \exp\left(-\frac{\Delta E_i - E_{\text{ref}}}{kT}\right) \quad (26)$$

in Eq. (22) has a peak value of $N_i \exp(-1)/kT_{\text{peak}i}$ at a peak temperature

$$T_{\text{peak}i} = \frac{\Delta E_i - E_{\text{ref}}}{k}. \quad (27)$$

Although the actual $T_{\text{peak}i}$ of $H(T, E_{\text{ref}})$ is slightly different from the $T_{\text{peak}i}$ calculated by Eq. (27) due to the temperature dependence of $I(\Delta E_{Di})$, we can easily determine the accurate values of $(N_{Di}$ and $\Delta E_{Di})$ or $(N_{TEi}$ and $\Delta E_{TEi})$ from the peak of the experimental $H(T, E_{\text{ref}})$, using a personal computer. The Windows application software for FCCS can be freely downloaded at our web site (<http://www.osakac.ac.jp/labs/matsuura/>). This software can also evaluate them by using the curve-fitting method, DHES, and the other methods mentioned in Section 2.

Let us consider the meaning of N_{comp} using Fig. 2. As the measurement temperature rises, the Fermi level moves from LowT to HighT in Fig. 2. In Fig. 2(a), the Fermi level crosses E_D in the temperature range of measurement. So, we can determine N_D and E_D . All the acceptors are negatively ionized. Therefore,

$$N_{\text{comp}} = N_A, \quad (28)$$

and N_{comp} is positive.

Because the Fermi level does not cross E_D in Fig. 2(b), we cannot determine E_D . All the donors are positively ionized, and all the acceptors are negatively ionized in the temperature range of measurement. Therefore

$$N_{\text{comp}} = N_A - N_D, \quad (29)$$

and N_{comp} is negative because the conduction type is n-type.

Because the Fermi level crosses E_{D2} and E_{D3} in Fig. 2(c), we can determine N_{D2} , E_{D2} , N_{D3} , and E_{D3} . All the donors with E_{D1} are positively ionized, and all the acceptors are negatively ionized in the temperature range of measurement. Because all the donors with E_{D4} are neutral, they do not affect the electron concentration in the measurement temperature range. Therefore

$$N_{\text{comp}} = N_A - N_{D1}. \quad (30)$$

Because the Fermi level crosses E_D , E_{TE1} , and E_{TE2} in Fig. 2(d), we can evaluate E_D , N_D , E_{TE1} , N_{TE1} , E_{TE2} , and N_{TE2} . All the electron traps with E_{TE3} are negatively ionized because they capture electrons, and all the acceptors are negatively ionized. Therefore

$$N_{\text{comp}} = N_A + \sum_{i=1}^3 N_{TEi} \quad (31)$$

and N_{comp} is positive. Here, electron traps are negative when they capture electrons, while they are neutral when they emit electrons.

Because the Fermi level crosses E_{TE1} and E_{TE2} in Fig. 2(e), we can evaluate E_{TE1} , N_{TE1} , E_{TE2} , and N_{TE2} . All the donors are positively ionized, all the electron traps with E_{TE3} are negatively ionized because they capture electrons, and all the acceptors are negatively ionized in the temperature range of measurement. Therefore

$$N_{\text{comp}} = N_A + \sum_{i=1}^3 N_{TEi} - N_D. \quad (32)$$

Using FCCS, the densities and energy levels are determined from $n(T)$ for the case of two donors shown by \diamond in Fig. 1. Figure 3(a) shows $H(T, 0)$ calculated by Eq. (21). The peak temperature and value of $H(T, 0)$ are 249 K and $1.93 \times 10^{36} \text{ cm}^{-6} \text{ eV}^{-2.5}$, from which the energy level (ΔE_{D1}) and density (N_{D1}) of the corresponding donor species are determined as 120.1 meV and $1.12 \times 10^{16} \text{ cm}^{-3}$.

In order to investigate another donor species included in this semiconductor, the FCCS signal of $H2(T, E_{\text{ref}})$, in which the influence of the previously determined donor species is removed, is calculated using the following equation. It is clear from Eq. (22) that

$$H2(T, E_{\text{ref}}) = \frac{n(T)^2}{(kT)^{5/2}} \exp\left(\frac{E_{\text{ref}}}{kT}\right) - \frac{N_{D1}}{kT} \exp\left(-\frac{\Delta E_{D1} - E_{\text{ref}}}{kT}\right) I(\Delta E_{D1}) \quad (33)$$

is not influenced by the donor with ΔE_{D1} . Figure 3(b) depicts $H2(T, 0.030754)$. Since a peak appears in this figure, another donor species is included. Using the peak temperature of 150.6 K and the peak value of $6.63 \times 10^{36} \text{ cm}^{-6} \text{ eV}^{-2.5}$, the donor level (ΔE_{D2}) and the donor density (N_{D2}) are determined as 81.3 meV and $5.08 \times 10^{15} \text{ cm}^{-3}$. The

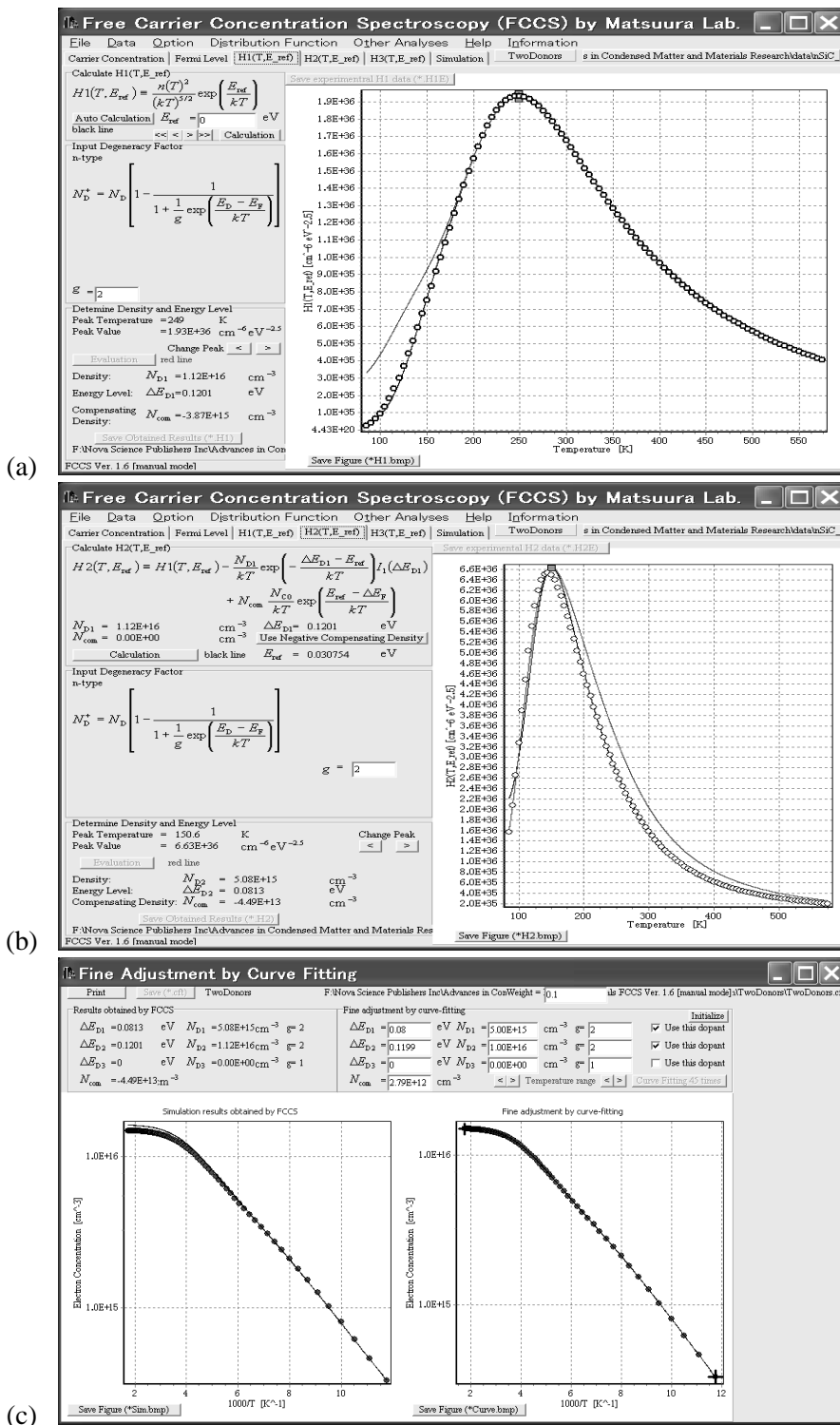


Figure 3. FCCS signal for case of two donors in Fig. 1; (a) $H(T, E_{ref})$, (b) $H2(T, E_{ref})$, and (c) curve fitting using values determined by FCCS.

FCCS signal of $H3(T, E_{\text{ref}})$, in which the influences of two donor species previously determined are removed, is calculated. However, $H3(T, E_{\text{ref}})$ is nearly zero, indicating that this semiconductor includes two types of donor species. Since this donor level is considered to be shallowest in the measurement temperature range, N_{comp} is determined to be $-4.49 \times 10^{13} \text{ cm}^{-3}$ from the value of the signal at the lowest temperature.

Since it is found that two types of donor species are included and the approximate values of ΔE_{D1} , N_{D1} , ΔE_{D2} , N_{D2} , and N_{comp} were estimated, the curve-fitting method can be carried out. Figure 3(c) shows the result by the curve-fitting procedure. By the fine adjustment, the values of ΔE_{D1} , N_{D1} , ΔE_{D2} , N_{D2} , and N_{comp} are finally determined to be 119.9 meV, $1.00 \times 10^{16} \text{ cm}^{-3}$, 80.0 meV, $5.00 \times 10^{15} \text{ cm}^{-3}$, and $2.79 \times 10^{12} \text{ cm}^{-3}$, respectively. The determined donor levels and densities are quite reasonable. Although N_{comp} determined by FCCS is not zero, the value is much less than the donor densities. It is, therefore, elucidated that FCCS can accurately determine the densities and energy levels of donors from $n(T)$.

3.2.2. p-type Semiconductors

From the charge neutrality condition, $p(T)$ can be written as [5]

$$p(T) = \sum_{i=1} N_{Ai} f_{\text{FD}}(\Delta E_{Ai}) - \sum_{j=1} N_{\text{TH}j} [1 - f_{\text{FD}}(\Delta E_{\text{TH}j})] - N_{\text{D}} \quad (34)$$

in the temperature range in which $n(T)$ is much less than $p(T)$, where $f_{\text{FD}}(\Delta E)$ is the Fermi-Dirac distribution function for acceptors and hole traps, which is given by [5]

$$f_{\text{FD}}(\Delta E) = \frac{1}{1 + 4 \exp \left(-\frac{\Delta E_{\text{F}}(T) - \Delta E}{kT} \right)}, \quad (35)$$

N_{Ai} and ΔE_{Ai} are the density and energy level measured from the valence band maximum (E_{V}) of an i th acceptor, respectively, $N_{\text{TH}j}$ and $\Delta E_{\text{TH}j}$ are the density and energy level measured from E_{V} of a j th hole trap, and $\Delta E_{\text{F}}(T)$ is the Fermi level measured from E_{V} at T .

On the other hand, using the effective density of states $N_{\text{V}}(T)$ in the valence band, $p(T)$ is expressed as [5]

$$p(T) = N_{\text{V}}(T) \exp \left(-\frac{\Delta E_{\text{F}}(T)}{kT} \right), \quad (36)$$

where

$$N_{\text{V}}(T) = N_{\text{V}0} k^{3/2} T^{3/2}, \quad (37)$$

$$N_{\text{V}0} = 2 \left(\frac{2\pi m_{\text{h}}^*}{h^2} \right)^{3/2}, \quad (38)$$

m_{h}^* is the hole effective mass.

The FCCS signal is defined as

$$H(T, E_{\text{ref}}) \equiv \frac{p(T)^2}{(kT)^{5/2}} \exp \left(\frac{E_{\text{ref}}}{kT} \right). \quad (39)$$

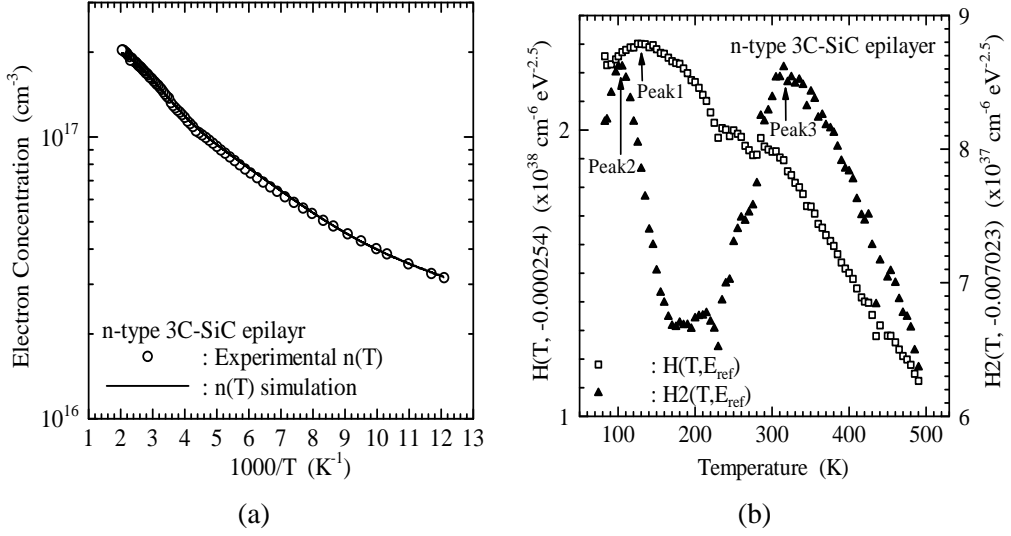


Figure 4. Temperature dependence of electron concentration for undoped 3C-SiC epilayer; (a) experimental and simulated $n(T)$ and (b) FCCS signals of $H(T, E_{\text{ref}})$ and $H^2(T, E_{\text{ref}})$.

Substituting Eq. (34) for one of the $p(T)$ in Eq. (39) and substituting Eq. (36) for the other $p(T)$ in Eq. (39) yield

$$\begin{aligned}
 H(T, E_{\text{ref}}) = & \sum_{i=1} \frac{N_{Ai}}{kT} \exp\left(-\frac{\Delta E_{Ai} - E_{\text{ref}}}{kT}\right) I_p(\Delta E_{Ai}) \\
 & + \sum_{j=1} \frac{N_{THj}}{kT} \exp\left(-\frac{\Delta E_{THj} - E_{\text{ref}}}{kT}\right) I_p(\Delta E_{THj}) \\
 & - \frac{N_{\text{comp}} N_{V0}}{kT} \exp\left(\frac{E_{\text{ref}} - \Delta E_F(T)}{kT}\right), \quad (40)
 \end{aligned}$$

where

$$I_p(\Delta E) = \frac{N_{V0}}{4 + \exp\left(\frac{\Delta E_F(T) - \Delta E}{kT}\right)} \quad (41)$$

and

$$N_{\text{comp}} = N_D + \sum_{j=1} N_{THj}. \quad (42)$$

3.3. Experimental Results and Discussion

3.3.1. Determination of Densities and Energy Levels of Dopants

Figure 4(a) shows the experimental $n(T)$ for an undoped n-type 3C-SiC epilayer [11], denoted by \bigcirc . Figure 4(b) depicts the FCCS signal of $H(T, -0.000254)$, denoted by \square . The peak temperature and value of $H(T, -0.000254)$ are 137.3 K and $2.30 \times 10^{38} \text{ cm}^{-6} \text{ eV}^{-2.5}$,

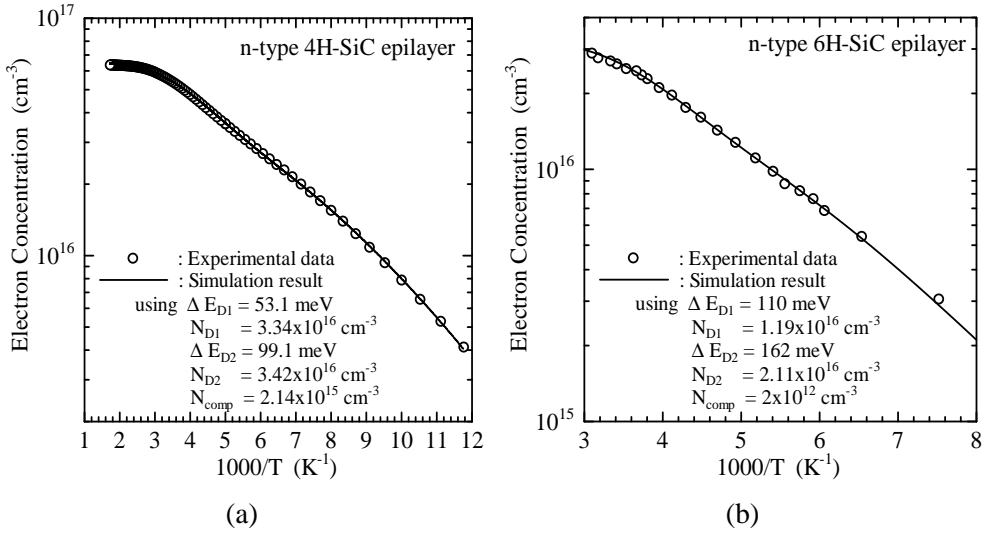


Figure 5. Experimental and simulated $n(T)$ for n-type 4H-SiC (a) and n-type 6H-SiC (b).

respectively, from which the energy level (ΔE_{D1}) and density (N_{D1}) of the corresponding donor species are determined to be 51.0 meV and $7.10 \times 10^{16} \text{ cm}^{-3}$, respectively.

Figure 4(b) also shows $H2(T, -0.007023)$, denoted by \blacktriangle . Since two peaks appear, other donor species are included in this epilayer. The low peak temperature and value of $H(T, 0.000254)$ are 98.4 K and $8.54 \times 10^{37} \text{ cm}^{-6} \text{ eV}^{-2.5}$, respectively, and the high peak temperature and value are 315 K and $8.61 \times 10^{37} \text{ cm}^{-6} \text{ eV}^{-2.5}$, respectively. The energy level (ΔE_{D2}) and density (N_{D2}) of the donor species corresponding to the peak at the low temperature are determined as 18.4 meV and $3.84 \times 10^{16} \text{ cm}^{-3}$, respectively, and the energy level (ΔE_{D3}) and density (N_{D3}) of the donor species corresponding to the peak at the high temperature are determined to be 113.9 meV and $1.07 \times 10^{17} \text{ cm}^{-3}$, respectively. However, $H3(T, E_{\text{ref}})$ is nearly zero, indicating that this epilayer includes three types of donor species. Since ΔE_{D2} is shallowest in the measurement temperature range, N_{comp} is determined to be $-1.98 \times 10^{15} \text{ cm}^{-3}$ from the value of $H2(T, E_{\text{ref}})$ at the lowest temperature.

In order to verify the values obtained by FCCS, the $n(T)$ is simulated using Eqs. (4) and (7). The solid line in Fig. 4(a) represents the $n(T)$ simulation, and is in good agreement with the experimental $n(T)$, indicating that the values determined by FCCS are reliable.

Suzuki *et al.* [12] insisted that the ~ 15 meV donor species came from nonstoichiometric defects in unintentionally doped films. From photoluminescence measurements, Freitas *et al.* [13] and Kaplan *et al.* [14] insisted that the substitutional N donor level was ~ 54 meV. On the other hand, the origin of the donor species with ΔE_{D3} is uncertain.

The open circles in Fig. 5 represent the experimental $n(T)$ and the solid line represents the $n(T)$ simulation with the values by FCCS, for n-type 4H-SiC (a) and 6H-SiC (b) epilayers. The solid lines are in good agreement with the experimental $n(T)$, indicating that the values determined by FCCS are reliable.

According to literature [15, 16], ΔE_{D1} and ΔE_{D2} correspond to the energy levels of

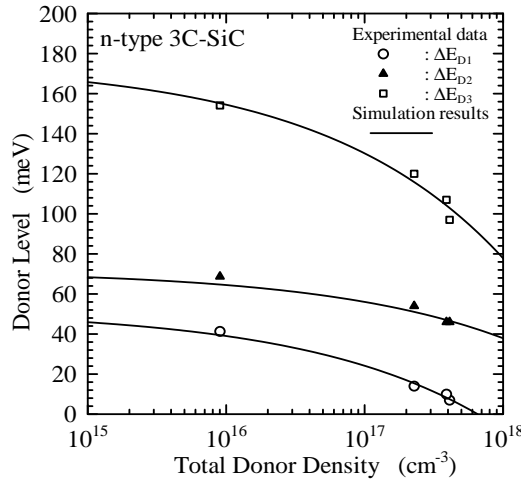


Figure 6. Dependence of each donor level on total donor density in n-type 3C-SiC.

isolated, substitutional N donors at hexagonal and cubic lattice sites in 4H-SiC or 6H-SiC, respectively. Because the ratio of the number of hexagonal lattice sites to the number of cubic lattice sites in 4H-SiC is unit, the probability for N atoms being put into each lattice site is found to be an half, which consists that the experimental result of $N_{D1} \simeq N_{D2}$. On the other hand, the ratio of the number of hexagonal lattice sites to the number of cubic lattice sites in 6H-SiC is 1 : 2, which consists that the experimental result of $2N_{D1} \simeq N_{D2}$.

The acceptor densities and energy levels in undoped GaSb and InGaSb epilayers as well as the donor density and energy level in Te-doped Al_{0.2}Ga_{0.8}Sb were determined [17, 18, 19].

3.3.2. Dopant-Density Dependence

Figure 6 shows the dependence of each donor level on a total donor density ($N_{D,\text{total}} \equiv N_{D1} + N_{D2} + N_{D3}$) [20]. The symbols of \circ , \blacktriangle and \square represent ΔE_{D1} , ΔE_{D2} and ΔE_{D3} , respectively. Figure 7(a) and (b) depict the dependence of each donor level in N-doped 4H-SiC epilayers on a total donor density ($N_{D,\text{total}} \equiv N_{D1} + N_{D2}$) [21] and the dependence of each acceptor level in Al-doped 4H-SiC epilayers on a total acceptor density ($N_{A,\text{total}} \equiv N_{A1} + N_{A2}$) [22], respectively. The symbols of \circ and \blacktriangle in Fig. 7(a) represent ΔE_{D1} and ΔE_{D2} , respectively, and the symbols of \circ and \blacktriangle in Fig. 7(b) represent ΔE_{A1} and ΔE_{A2} , respectively.

An ideal donor level $\Delta E_{Di}(0)$ is the energy required to emit one electron from the donor site into infinity on E_C . However, since an n-type semiconductor is electrically neutral, each positively charged donor is shielded by one electron on E_C . This shielding electron is assumed to be located within half (\bar{r}) of an average distance ($1/\sqrt[3]{N_{D,\text{total}}}$) of the donors, indicating that the donor level should be lowered by the energy higher than $q/(4\pi\epsilon_s\epsilon_0\bar{r})$ due to Coulomb's attraction. Therefore,

$$\Delta E_{Di}(N_{D,\text{total}}) = \Delta E_{Di}(0) - \alpha_{Di} \sqrt[3]{N_{D,\text{total}}} \quad (43)$$

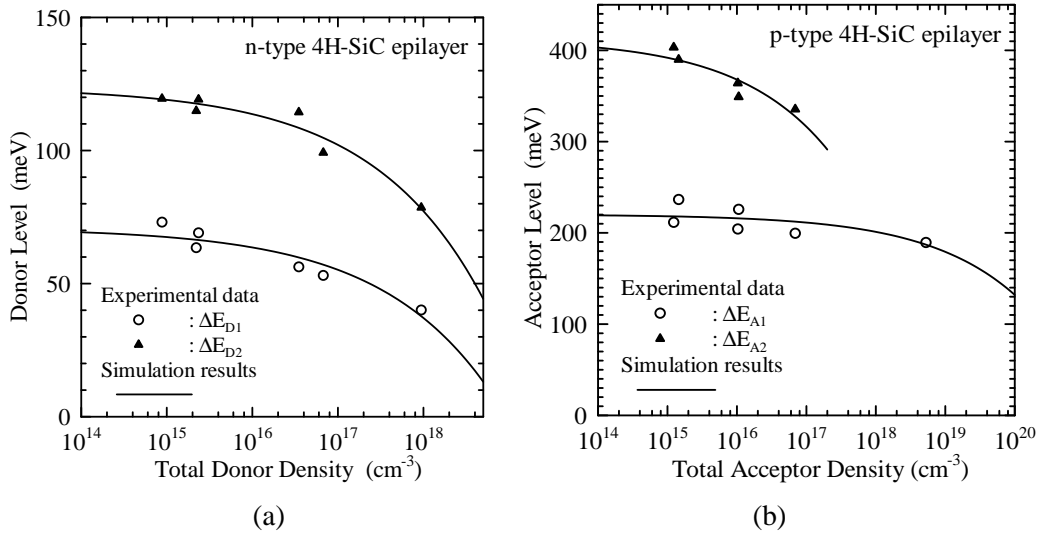


Figure 7. Dependence of each dopant level on total dopant density in 4H-SiC; (a) donors and (b) acceptors.

and

$$\alpha_{Di} \gtrsim \frac{q}{8\pi\epsilon_s\epsilon_0} = 2.44 \times 10^{-5} \text{ meV} \cdot \text{cm}. \quad (44)$$

where ϵ_0 is the free space permittivity, and ϵ_s is the dielectric constant for SiC. On the other hand,

$$\Delta E_{Ai}(N_{A,\text{total}}) = \Delta E_{Ai}(0) - \alpha_{Ai} \sqrt[3]{N_{A,\text{total}}}. \quad (45)$$

In N-doped n-type 3C-SiC and 4H-SiC, the fitting parameters obtained by a least-squares fit of Eq. (43) to the data in Fig. 6 and Fig. 7(a) are listed in Table 1, respectively, and the $\Delta E_{Di}(N_{D,\text{total}})$ simulations are denoted by the solid lines in Fig. 6 and Fig. 7(a). Since these α_{Di} are satisfied with Eq. (44), they are considered to be reasonable. In Al-doped p-type 4H-SiC, the fitting parameters obtained by a least-squares fit of Eq. (45) to the data in Fig. 7(b) are listed in Table 1, and the $\Delta E_{Ai}(N_{A,\text{total}})$ simulations are denoted by the lines in Fig. 7(b). Although these α_{Ai} are a little lower than $2.44 \times 10^{-5} \text{ meV} \cdot \text{cm}$, they are considered to be reasonable.

Figure 8(a) and (b) show the temperature dependence of the electron mobility and the hole mobility, respectively. As is clear from Fig. 8(a), the electron mobility at $> 250 \text{ K}$ can be expressed as

$$\mu_e(T, N_{\text{imp}}) = \mu_e(300, N_{\text{imp}}) \left(\frac{T}{300} \right)^{-\beta_e(N_{\text{imp}})}, \quad (46)$$

where $N_{\text{imp}} = N_{D1} + N_{D2} + N_A$. Therefore, $\mu_e(300, N_{\text{imp}})$ and $\beta_e(N_{\text{imp}})$ can be evaluated individually as follows.

$$\beta_e(N_{\text{imp}}) = \beta_e^{\min} + \frac{\beta_e^{\max} - \beta_e^{\min}}{1 + \left(\frac{N_{\text{imp}}}{N_e^\beta} \right)^{\gamma_e^\beta}}, \quad (47)$$

Table 1. Parameters for donor levels and acceptor in SiC.

Parameters	N-doped 3C-SiC	N-doped 4H-SiC	Al-doped 4H-SiC
$\Delta E_{D1}(0)$ (meV)	51.9	70.9	—
α_{D1} (meV·cm)	5.97×10^{-5}	3.38×10^{-5}	—
$\Delta E_{D2}(0)$ (meV)	71.8	123.7	—
α_{D2} (meV·cm)	3.38×10^{-5}	4.65×10^{-5}	—
$\Delta E_{D3}(0)$ (meV)	176	—	—
α_{D3} (meV·cm)	9.77×10^{-5}	—	—
$\Delta E_{A1}(0)$ (meV)	—	—	220
α_{A1} (meV·cm)	—	—	1.90×10^{-5}
$\Delta E_{A2}(0)$ (meV)	—	—	413
α_{A2} (meV·cm)	—	—	2.07×10^{-5}

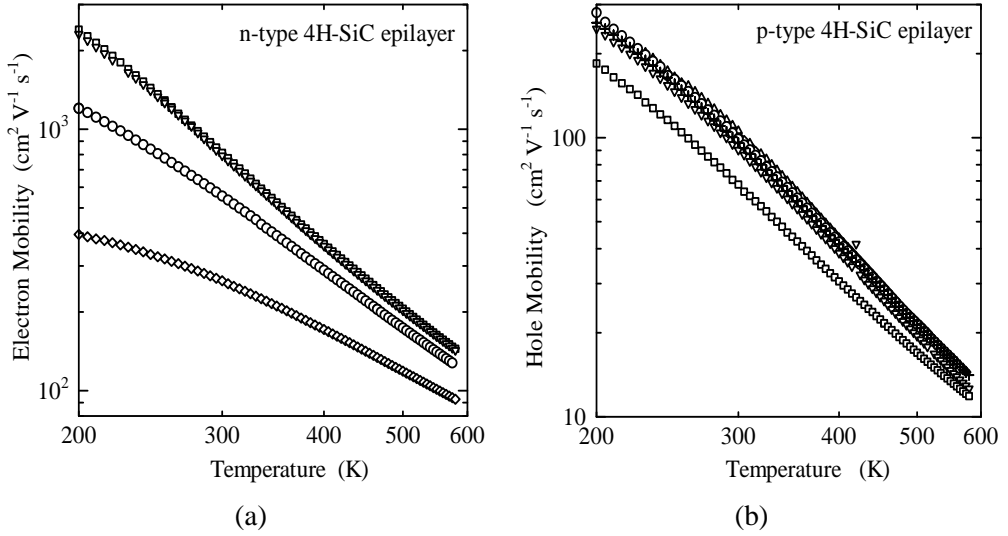


Figure 8. Temperature dependencies of electron mobility for n-type 4H-SiC epilayers (a) and hole mobility for p-type 4H-SiC epilayers (b).

and

$$\mu_e(300, N_{\text{imp}}) = \mu_e^{\min}(300) + \frac{\mu_e^{\max}(300) - \mu_e^{\min}(300)}{1 + \left(\frac{N_{\text{imp}}}{N_e^{\mu}}\right)^{\gamma_e^{\mu}}}, \quad (48)$$

where β_e^{\min} , β_e^{\max} , N_e^{β} , γ_e^{β} , $\mu_e^{\min}(300)$, $\mu_e^{\max}(300)$, N_e^{μ} , and γ_e^{μ} are the fitting parameters. In Fig. 8(b), moreover, the hole mobility at > 250 K can be expressed as

$$\mu_h(T, N_{\text{imp}}) = \mu_h(300, N_{\text{imp}}) \left(\frac{T}{300}\right)^{-\beta_h(N_{\text{imp}})}, \quad (49)$$

where $N_{\text{imp}} = N_{\text{A1}} + N_{\text{A2}} + N_{\text{D}}$. Therefore, $\mu_{\text{h}}(300, N_{\text{imp}})$ and $\beta_{\text{h}}(N_{\text{imp}})$ can be evaluated individually as follows.

$$\beta_{\text{h}}(N_{\text{imp}}) = \beta_{\text{h}}^{\min} + \frac{\beta_{\text{h}}^{\max} - \beta_{\text{h}}^{\min}}{1 + \left(\frac{N_{\text{imp}}}{N_{\text{h}}^{\beta}} \right)^{\gamma_{\text{h}}^{\beta}}}, \quad (50)$$

and

$$\mu_{\text{h}}(300, N_{\text{imp}}) = \mu_{\text{h}}^{\min}(300) + \frac{\mu_{\text{h}}^{\max}(300) - \mu_{\text{h}}^{\min}(300)}{1 + \left(\frac{N_{\text{imp}}}{N_{\text{h}}^{\mu}} \right)^{\gamma_{\text{h}}^{\mu}}}, \quad (51)$$

where β_{h}^{\min} , β_{h}^{\max} , N_{h}^{β} , $\gamma_{\text{h}}^{\beta}$, $\mu_{\text{h}}^{\min}(300)$, $\mu_{\text{h}}^{\max}(300)$, N_{h}^{μ} , and γ_{h}^{μ} are the fitting parameters.

Table 2. Parameters for $\beta(N_{\text{imp}})$.

β_{e}^{\min}	β_{e}^{\max}	$N_{\text{e}}^{\beta} (\text{cm}^{-3})$	$\gamma_{\text{e}}^{\beta}$	β_{h}^{\min}	β_{h}^{\max}	$N_{\text{h}}^{\beta} (\text{cm}^{-3})$	$\gamma_{\text{h}}^{\beta}$
1.54	2.62	1.14×10^{17}	1.35	2.51	3.04	8.64×10^{17}	0.456

Table 3. Parameters for $\mu(300, N_{\text{imp}})$.

$\mu_{\text{e}}^{\min} [\text{cm}^2/(\text{V}\cdot\text{s})]$	$\mu_{\text{e}}^{\max} [\text{cm}^2/(\text{V}\cdot\text{s})]$	$N_{\text{e}}^{\mu} (\text{cm}^{-3})$	γ_{e}^{μ}
0	977	1.17×10^{17}	0.49
$\mu_{\text{h}}^{\min} [\text{cm}^2/(\text{V}\cdot\text{s})]$	$\mu_{\text{h}}^{\max} [\text{cm}^2/(\text{V}\cdot\text{s})]$	$N_{\text{h}}^{\mu} (\text{cm}^{-3})$	γ_{h}^{μ}
37.6	106.0	2.97×10^{18}	0.356

From Fig. 8(a), all the parameters in Eqs. (47) and (48) were determined, and are listed in Tables 2 and 3. From Fig. 8(b), on the other hand, all the parameters in Eqs. (50) and (51) were determined, and are listed in Tables 2 and 3. Therefore, the electron and hole mobilities for any N_{imp} at $T > 250$ K can be simulated.

Figure 9(a) shows $p(T)$ for three different Al concentrations [22, 23]. One acceptor level was approximately $E_{\text{V}} + 0.22$ eV, which is assigned to an Al acceptor. Therefore, the density and energy level of this acceptor are represented by N_{A1} and E_{A1} , respectively. The other acceptor level, on the other hand, was approximately $E_{\text{V}} + 0.38$ eV, which has not been assigned. The density and energy level of the deep acceptor are represented by N_{DA} and E_{DA} , respectively. Figure 9(b) shows the relationship between N_{A1} and N_{DA} . From the figure, the following empirical relationship between N_{A1} and N_{DA} was obtained;

$$N_{\text{DA}} = 0.6 \times N_{\text{A1}}. \quad (52)$$

Therefore, it is considered that the deep acceptor is most likely related to Al.

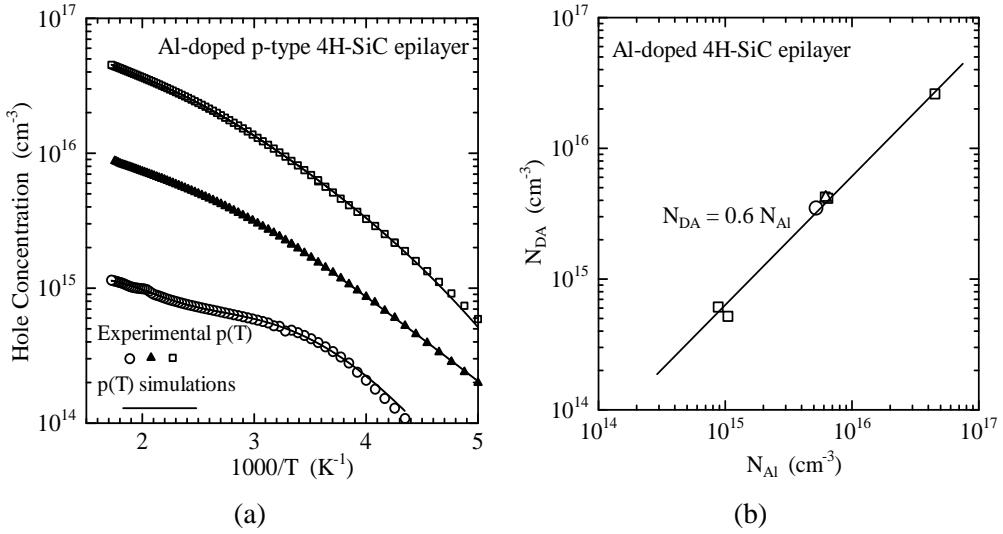


Figure 9. Temperature dependence of hole concentration for three different Al-doping levels (a) and relationship between Al acceptor density and deep acceptor density (b).

3.4. Electron-irradiated 4H-SiC

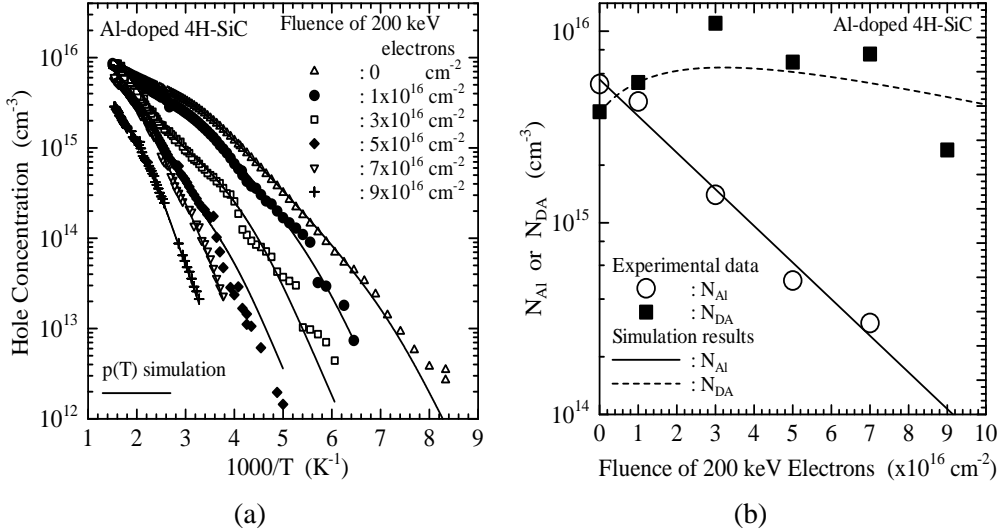


Figure 10. Al-doped p-type 4H-SiC epilayer irradiated by 200 keV electron irradiation; (a) temperature dependencies of hole concentration before and after irradiation and (b) fluence dependencies of Al acceptor and deep acceptor densities.

Figure 10(a) shows the experimental $p(T)$ in a $10 \mu\text{m}$ -thick Al-doped p-type 4H-SiC epilayer on n-type 4H-SiC (thickness: $376 \mu\text{m}$, with a resistivity of $0.02 \Omega\text{cm}$) for fluences (Φ) of 0 (Δ), 1×10^{16} (\bullet), 3×10^{16} (\square), 5×10^{16} (\blacklozenge), 7×10^{16} (∇), and $9 \times 10^{16} \text{ cm}^{-2}$ (+),

respectively [24]. The $p(T)$ at low temperatures decreased significantly with increasing Φ , whereas the $p(T)$ at high temperatures was changed slightly by the irradiation.

In Fig. 10(a), \triangle represents $p(T)$ for the unirradiated case, and the solid line is the $p(T)$ simulation with N_{Al} of $5.3 \times 10^{15} \text{ cm}^{-3}$, E_{Al} of $E_{\text{V}} + 0.20 \text{ eV}$, N_{DA} of $3.7 \times 10^{15} \text{ cm}^{-3}$, E_{DA} of $E_{\text{V}} + 0.37 \text{ eV}$, and N_{comp} of $2 \times 10^{13} \text{ cm}^{-3}$, which were determined by FCCS. Since the $p(T)$ simulation is in good agreement with the experimental $p(T)$ for the unirradiated case, the values obtained by FCCS are reliable.

Figure 10(b) shows the fluence dependencies of N_{Al} and N_{DA} , denoted by \bigcirc and \blacksquare , respectively. N_{Al} decreased with increasing Φ , and finally there are no more Al acceptors. On the other hand, N_{DA} initially increased with Φ , and then decreased.

200 keV electron irradiation can replace substitutional C atoms (C_s) [23]. In order to reduce N_{Al} by the 200 keV electron irradiation, the surroundings of the Al acceptor need to be changed. This indicates that the rate of decrease of N_{Al} by the irradiation is proportional to N_{Al} . Consequently, the differential equation that leads to fluence dependence of Al acceptors $N_{\text{Al}}(\Phi)$ is given by

$$\frac{dN_{\text{Al}}(\Phi)}{d\Phi} = -\kappa_{\text{Al}}N_{\text{Al}}(\Phi), \quad (53)$$

where κ_{Al} is the removal cross section of Al acceptors for 200 keV electron irradiation. Therefore,

$$N_{\text{Al}}(\Phi) = N_{\text{Al}}(0) \exp(-\kappa_{\text{Al}}\Phi). \quad (54)$$

Figure 10(b) shows $N_{\text{Al}}(\Phi)$ in a semi-logarithmic scale, and the solid line is a straight line obtained by least-squares fitting. Since the straight line is in good agreement with \bigcirc in the semi-logarithmic plots, Eq. (54) is feasible for the fluence dependence of N_{Al} . κ_{Al} is then determined from the slope as $4.4 \times 10^{-17} \text{ cm}^2$.

In Fig. 10(b), at fluences of $\leq 3 \times 10^{16} \text{ cm}^{-2}$, N_{DA} increased with increasing Φ , while N_{Al} decreased. Furthermore, the increment of N_{DA} is close to the decrement of N_{Al} . This experimental result may indicate that the 200 keV electron irradiation transforms the Al acceptor into the deep acceptor. In this case, the differential equation describing the fluence dependence of the deep acceptor density $N_{\text{DA}}(\Phi)$ can be expressed as

$$\frac{dN_{\text{DA}}(\Phi)}{d\Phi} = -\frac{dN_{\text{Al}}(\Phi)}{d\Phi} - \kappa_{\text{DA}}N_{\text{DA}}(\Phi), \quad (55)$$

where κ_{DA} is the removal cross section of the deep acceptors for 200 keV electron irradiation. The broken line in Fig. 10(b) represents the simulated $N_{\text{DA}}(\Phi)$ with κ_{DA} of $1.0 \times 10^{-17} \text{ cm}^2$ using Eq. (55), which shows qualitative agreement with the experimental data, but not quantitative agreement.

Figure 11(a) shows the experimental $n(T)$ before irradiation (\bigcirc) and after irradiation with 200 keV electrons at Φ of $1 \times 10^{16} \text{ cm}^{-2}$ (\blacktriangle) and $2 \times 10^{16} \text{ cm}^{-2}$ (\square). From each $n(T)$, two types of donor species were detected and evaluated using FCCS. The energy level of N donors at hexagonal C-sublattice sites (E_{NH}) was $E_{\text{C}} - 70 \text{ meV}$. The energy level of N donors at cubic C-sublattice sites (E_{NK}) was $E_{\text{C}} - 120 \text{ meV}$. Figure 11(b) shows the fluence dependencies of N_{NH} (\bigcirc) and N_{NK} (\blacksquare). The N_{NH} decreased substantially with increasing Φ of 200 keV electrons, whereas N_{NK} decreased only slightly, indicating that N donors at hexagonal C-sublattice sites are less radiation-resistant than N donors at cubic C-sublattice

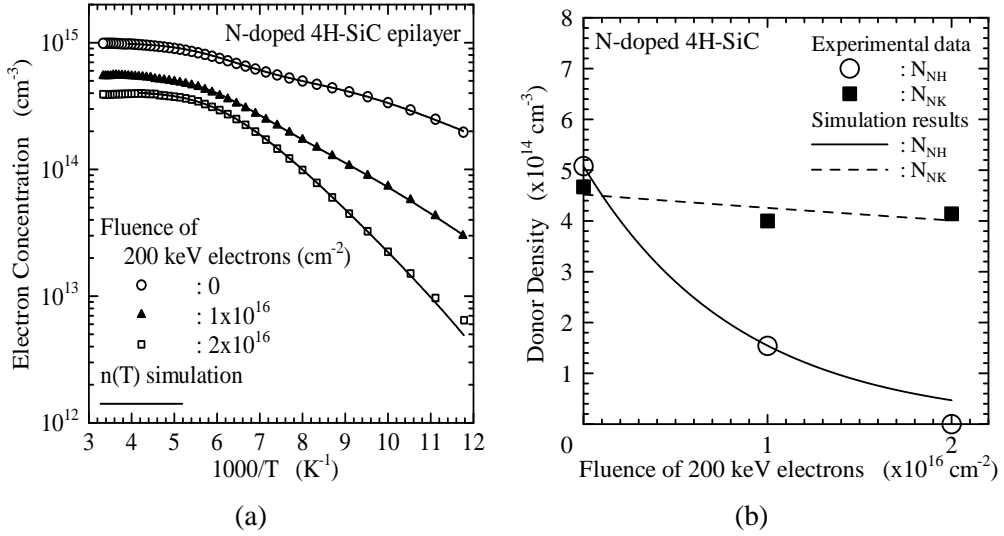


Figure 11. N-doped n-type 4H-SiC epilayer irradiated by 200 keV electron irradiation; (a) temperature dependencies of electron concentration before and after irradiation and (b) fluence dependencies of N donors located at hexagonal and cubic C-sublattice sites.

sites. This finding suggests that 3C-SiC might be the most and 6H-SiC should be the least radiation-resistant of N-doped 3C-SiC, 4H-SiC, and 6H-SiC.

By analogy with Eq. (54), the fluence dependencies of N_{NH} and N_{NK} are expected to be derived from the following differential equations:

$$\frac{dN_{NH}}{d\Phi} = -\kappa_{NH200}N_{NH} \quad (56)$$

and

$$\frac{dN_{NK}}{d\Phi} = -\kappa_{NK200}N_{NK}, \quad (57)$$

where κ_{NH200} and κ_{NK200} are the removal cross sections for 200 keV electron irradiation of the N donors at hexagonal and cubic C-sublattice sites, respectively. By fitting the curve to the experimental data, the values of κ_{NH200} and κ_{NK200} were determined to be 1.2×10^{-16} and $6.0 \times 10^{-18} \text{ cm}^2$, respectively. The solid and broken curves in Fig. 11(b) represent the simulated fluence dependencies of N_{NH} and N_{NK} , respectively.

3.5. Trap Densities Higher Than Dopant Density

Figure 12(a) shows the $p(T)$ for the 10 $\Omega \text{ cm}$ B-doped FZ-Si irradiated with several fluences of 10 MeV protons [25]. The \diamond , \triangle , \square , and \circ symbols correspond to the fluences of 0, 1.0×10^{13} , 1.0×10^{14} , and $2.5 \times 10^{14} \text{ cm}^{-2}$, respectively. Figure 12(b) shows the dependencies of B acceptor density and hole-trap densities on proton fluence. The values of ΔE_{TH1} , ΔE_{TH2} , and ΔE_{TH3} were $\sim 95 \text{ meV}$, $\sim 160 \text{ meV}$, and $\sim 300 \text{ meV}$, respectively.

The values of the lowest $\Delta E_F(T)$ in the temperature range of the measurement were 95, 97, 162, and 310 meV for the samples irradiated with fluences of 0, 1.0×10^{13} , 1.0×10^{14} ,

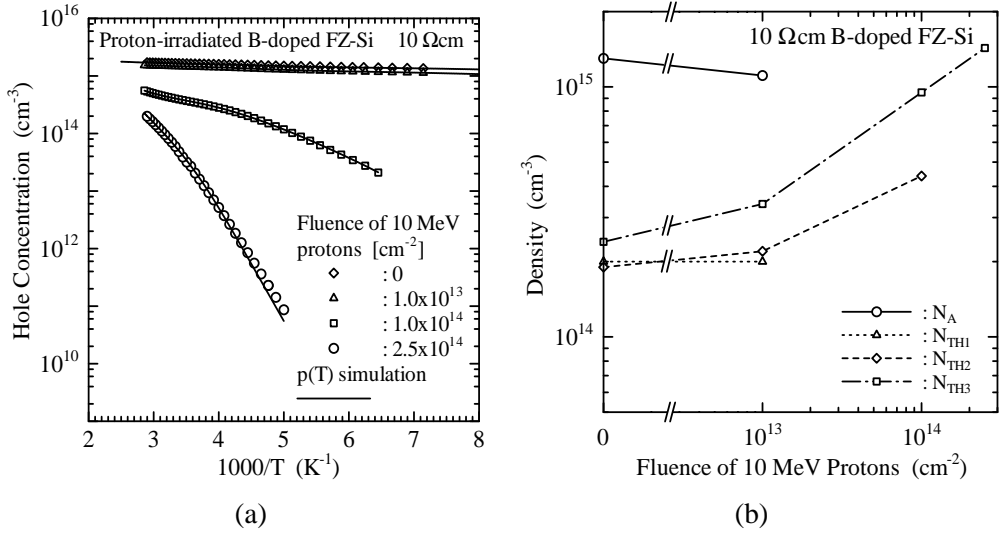


Figure 12. Proton-irradiated Si; (a) temperature dependencies of electron concentration in Si before and after proton irradiation and (b) fluence dependencies of densities of B acceptor and hole traps.

and $2.5 \times 10^{14} \text{ cm}^{-2}$, respectively. Since ΔE_A of B in Si is $\sim 45 \text{ meV}$, B acceptors were completely ionized at the lowest measurement temperature, indicating that ΔE_A could not be determined in this measurement temperature range. Because in the case of $1.0 \times 10^{14} \text{ cm}^{-2}$ fluence the hole traps with ΔE_{TH1} were not filled with holes at all in the measurement temperature range, the values of ΔE_{TH1} and N_{TH1} could not be evaluated. For the same reason, the values of ΔE_{TH1} , N_{TH1} , ΔE_{TH2} , and N_{TH2} could not be estimated in the sample irradiated with the $2.5 \times 10^{14} \text{ cm}^{-2}$ fluence.

The values of N_{TH2} and N_{TH3} increase clearly. Moreover, N_{TH3} of the sample irradiated with $2.5 \times 10^{14} \text{ cm}^{-2}$ exceeds N_A of the unirradiated sample. Because the density and energy level of the hole trap with a density higher than the acceptor density can be determined from FCCS, FCCS is superior to DLTS from the viewpoint of the evaluation of traps with high densities.

4. Nondegenerate Heavily-Doped Wide Bandgap Semiconductors

4.1. Problems of Heavily-Doped Case

The excited states of a substitutional dopant in a semiconductor have been theoretically discussed using the hydrogenic model (or the effective mass approximation) [26, 27, 28], and the existence of excited states of the dopant (e.g., B or P) in Si or Ge was experimentally confirmed from infrared absorption measurements at very low temperatures [26]. However, the influence of the excited states on the majority-carrier concentration in Si or Ge was not experimentally confirmed [27, 29], partially because the excited state levels of the dopants

in Si or Ge were too shallow and partially because $E_F(T)$ was deeper than the dopant energy level in the temperature range of the measurement. Therefore, by a least squares fit of the charge neutrality equation to the temperature dependence of the majority-carrier concentration experimentally obtained by Hall-effect measurements, the values of dopant density, dopant energy level, and compensating density can be determined using the Fermi-Dirac (FD) distribution function, which does not include the influence of the excited states of the dopant. The FD distribution functions for donors and acceptors are expressed as [5]

$$f_{\text{FD}}(E_D) = \frac{1}{1 + \frac{1}{g_{D,\text{FD}}} \exp\left(-\frac{E_F(T) - E_D}{kT}\right)} \quad (58)$$

and

$$f_{\text{FD}}(E_A) = \frac{1}{1 + g_{A,\text{FD}} \exp\left(-\frac{E_F(T) - E_A}{kT}\right)}, \quad (59)$$

respectively, where $g_{D,\text{FD}}$ and $g_{A,\text{FD}}$ are the degeneracy factors for donors and acceptors, respectively.

Because in p-type wide bandgap semiconductors the experimentally obtained values of E_A have been reported to be deep, $E_F(T)$ is often between E_A and E_V . Furthermore, because the excited state levels of acceptors are as deep as a B acceptor level (i.e., ground-state level) in Si, $E_F(T)$ is close to the excited state levels. The excited states of the acceptor must, therefore, affect $p(T)$.

Using a distribution function including the influence of the excited states of an acceptor derived from the viewpoint of the grand canonical ensemble [27, 30, 31], N_A was determined by fitting the simulation $p(T)$ to the experimental $p(T)$. The N_A determined this way was, however, much higher than the concentration of acceptor atoms determined by secondary ion mass spectroscopy (SIMS). This same situation occurred in the case of the FD distribution function [32, 33].

4.2. Experimental Results

Figure 13 shows $p(T)$ and $E_F(T)$ for the B-doped diamond. Because E_A of B in diamond is approximately $E_V + 0.35$ eV, $E_F(T)$ values were lower than E_A over the measurement temperature range.

N_A and E_A of B, and N_D can be determined using

$$p(T) = N_A F(E_A) - N_D, \quad (60)$$

where $n(T)$ is much less than $p(T)$ over the measurement temperature range, and $F(E_A)$ is the distribution function for acceptors. By replacing $F(E_A)$ with $f_{\text{FD}}(E_A)$, the values of N_A , E_A , and N_D were determined by FCCS and are listed in Table 4. In the table, f_{FD} , f_{MC} , and f_{GC} represent the FD distribution function and the distribution functions including the influence of the excited states of a dopant, which are derived from the viewpoint of the microcanonical (MC) and grand canonical (GC) ensembles, respectively, and C is the dopant concentration.

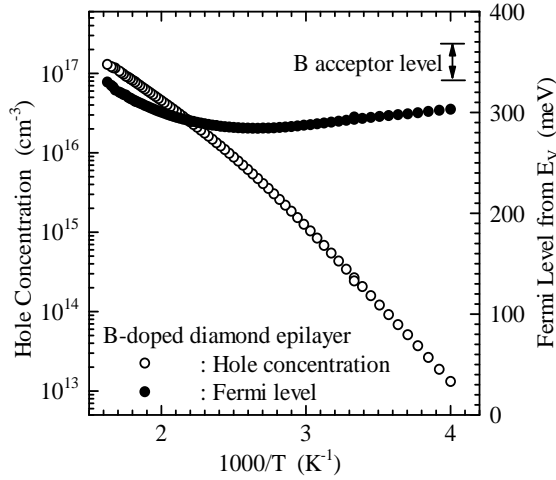


Figure 13. Temperature dependencies of hole concentration and Fermi level for B-doped diamond.

The N_A of $9.7 \times 10^{17} \text{ cm}^{-3}$ for $f_{\text{FD}}(E_A)$ is approximately five times higher than the B concentration (C_B) of approximately $2 \times 10^{17} \text{ cm}^{-3}$ determined by SIMS. Since N_A is the density of B atoms at the lattice sites, N_A should be less than or equal to C_B . Therefore, $f_{\text{FD}}(E_A)$ seems inappropriate to a distribution function for B acceptors in heavily-doped diamond.

Figure 14(a) shows $p(T)$ and $E_F(T)$ for the heavily Al-doped 6H-SiC wafer, while Fig. 14(b) shows $p(T)$ and $E_F(T)$ for the lightly Al-doped 6H-SiC epilayer. $E_F(T)$ values for the heavily-doped 6H-SiC were below E_A over the measurement temperature range, whereas $E_F(T)$ values for the lightly-doped 6H-SiC were above E_A over almost all the measurement temperature range.

The values of N_A , E_A , and N_D for $f_{\text{FD}}(E_A)$ were estimated and are listed in Table 4. The N_A obtained for the heavily-doped 6H-SiC is $2.5 \times 10^{19} \text{ cm}^{-3}$ that is approximately six times higher than the Al concentration (C_{Al}). On the other hand, the N_A obtained for the lightly-doped 6H-SiC is $5.1 \times 10^{15} \text{ cm}^{-3}$, which is nearly equal to the C_{Al} . This suggests that $f_{\text{FD}}(E_A)$ can be used only in the lightly doped sample.

As is clear from Table 4, in the Al implanted 4H-SiC layer the N_A of $4.9 \times 10^{19} \text{ cm}^{-3}$ is approximately five times higher than the C_{Al} , and in the Mg doped GaN epilayer the N_A of $8.5 \times 10^{19} \text{ cm}^{-3}$ is approximately four times higher than the Mg concentration (C_{Mg}).

4.3. Distribution Function for a Deep Substitutional Dopant

4.3.1. The Number of Configurations of the System

We now consider the microcanonical ensemble. Electrons and holes in semiconductors are fermions, which obey the Pauli exclusion principle. Because of this, in the allowed bands, the multiplicity function $W_B(E_i)$ for $n_e(E_i)$ electrons arranged in $D(E_i)$ states at a given

Table 4. Results for each distribution function.

	B-doped diamond	Heavily Al-doped 6H-SiC	Lightly Al-doped 6H-SiC	Al-implanted 4H-SiC	Mg-doped GaN
f_{MC}					
N_A (cm ⁻³)	2.8×10^{17}	3.0×10^{18}	4.4×10^{15}	1.2×10^{19}	6.0×10^{18}
E_A (eV)	$E_V + 0.32$	$E_V + 0.18$	$E_V + 0.20$	$E_V + 0.18$	$E_V + 0.16$
N_D (cm ⁻³)	2.0×10^{16}	9.7×10^{16}	3.7×10^{14}	2.2×10^{17}	1.3×10^{17}
f_{FD}					
N_A (cm ⁻³)	9.7×10^{17}	2.5×10^{19}	5.1×10^{15}	4.9×10^{19}	8.5×10^{19}
E_A (eV)	$E_V + 0.34$	$E_V + 0.18$	$E_V + 0.19$	$E_V + 0.16$	$E_V + 0.15$
N_D (cm ⁻³)	4.0×10^{16}	7.3×10^{17}	8.1×10^{14}	2.5×10^{18}	2.3×10^{18}
f_{GC}					
N_A (cm ⁻³)	2.1×10^{18}	3.8×10^{20}	5.2×10^{15}	4.9×10^{20}	2.7×10^{20}
E_A (eV)	$E_V + 0.38$	$E_V + 0.18$	$E_V + 0.19$	$E_V + 0.17$	$E_V + 0.17$
N_D (cm ⁻³)	1.4×10^{16}	1.2×10^{19}	8.4×10^{14}	1.7×10^{19}	2.6×10^{18}
Dopant concentration					
C (cm ⁻³)	$\sim 2 \times 10^{17}$	$\sim 4 \times 10^{18}$	$\sim 6 \times 10^{15}$	$\sim 1 \times 10^{19}$	$\sim 2 \times 10^{19}$

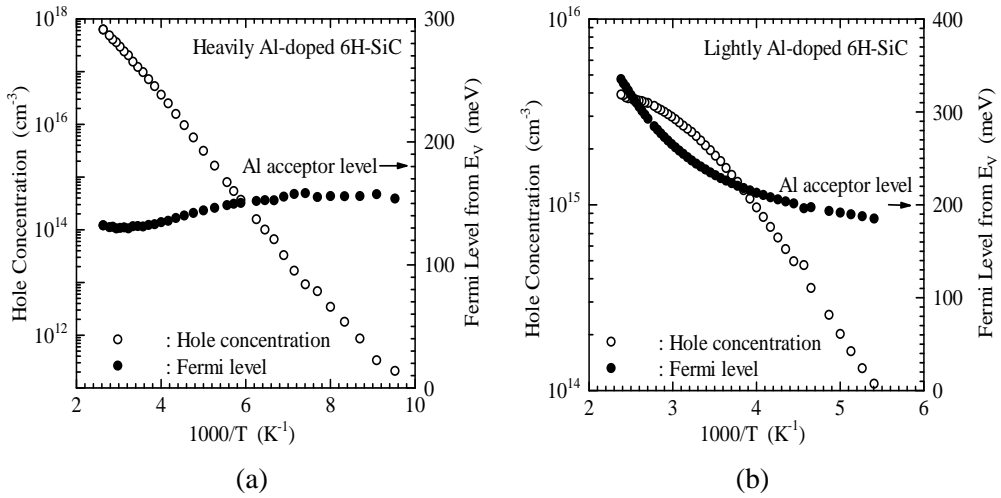


Figure 14. Temperature dependencies of hole concentration and Fermi level; (a) for heavily Al doped 6H-SiC and (b) for lightly Al doped 6H-SiC.

energy (E_i) is expressed as [30]

$$W_B(E_i) = \frac{D(E_i)!}{[D(E_i) - n_e(E_i)]! \cdot n_e(E_i)!}, \quad (61)$$

where $D(E_i)$ is the number of degenerate states per unit volume at E_i and $n_e(E_i)$ is the number of electrons per unit volume at E_i .

In a forbidden band, on the other hand, the multiplicity function for n_D electrons arranged in N_D donors is quite different from Eq. (61), where n_D is the number of electrons bound to donors per unit volume. When spin degeneracy as well as the excited states of the donor is neglected, the multiplicity function (W_{D1}) for the n_D electrons arranged in the N_D donors is given by

$$W_{D1} = \frac{N_D!}{(N_D - n_D)! \cdot n_D!} . \quad (62)$$

Each state, ground or excited, consists of a spin-up state and a spin-down state. When the energy difference between the two states in a magnetic field is denoted by ΔE_{spin} , the multiplicity function (W_{D2}) is given by

$$W_{D2} = \left[1 + \exp \left(-\frac{\Delta E_{\text{spin}}}{kT} \right) \right]^{n_D} . \quad (63)$$

When the magnetic field is zero or very weak ($\Delta E_{\text{spin}} \cong 0$),

$$W_{D2} \cong 2^{n_D} . \quad (64)$$

In a neutral donor, furthermore, only an electron is located at one state for the ground and excited states of the donor. The multiplicity function (W_{D3}) is given by

$$W_{D3} = \left[g_1 + \sum_{r=2}^l g_r \exp \left(-\frac{E_{r,D} - E_D}{kT} \right) \right]^{n_D} , \quad (65)$$

where $E_{r,D}$ is the $(r - 1)$ th excited state level ($r \geq 2$) of the donor, g_1 is the ground-state degeneracy factor of 1, g_r is the $(r - 1)$ th excited state degeneracy factor of r^2 , and the value of $(l - 1)$ is the highest order of the excited states considered here.

Consequently, the multiplicity function (W_D) for the n_D electrons arranged in the N_D donors is expressed as

$$W_D = W_{D1} W_{D2} W_{D3} . \quad (66)$$

Finally, the total number of configurations of the system (W) is obtained from the product of these multiplicities as

$$W = W_D \prod_i W_{Bi} . \quad (67)$$

4.3.2. Thermal Equilibrium Configuration

Thermal equilibrium configuration occurs when the entropy

$$S = k \ln W \quad (68)$$

reaches a maximum value under the following two conservation laws; (1) the total number (n_{total}) of electrons in the system is conserved, that is,

$$n_{\text{total}} = n_D + \sum_i n(E_i) = \text{const} \quad (69)$$

and (2) the total energy (E_{total}) of electrons in the system is conserved, i.e.,

$$E_{\text{total}} = \overline{E_D(T)} \cdot n_D + \sum_i E_i \cdot n(E_i) = \text{const}, \quad (70)$$

where $\overline{E_D(T)}$ is the average donor level given by

$$\overline{E_D(T)} = E_D + \overline{E_{\text{ex},D}(T)}, \quad (71)$$

and $\overline{E_{\text{ex},D}(T)}$ is the ensemble average of the ground and excited state levels of the donor, measured from E_D , and is given by

$$\overline{E_{\text{ex},D}(T)} = \frac{\sum_{r=2}^l (E_{r,D} - E_D) g_r \exp\left(-\frac{E_{r,D} - E_D}{kT}\right)}{1 + \sum_{r=2}^l g_r \exp\left(-\frac{E_{r,D} - E_D}{kT}\right)}. \quad (72)$$

Under these conditions, the distribution functions for electrons including the influence of the excited states of the donor $f_{\text{MC}}(E_D)$ can be derived [34].

$$f_{\text{MC}}(E_D) \equiv \frac{n_D}{N_D} = \frac{1}{1 + \frac{1}{g_{D,\text{MC}}(T)} \exp\left(-\frac{E_F(T) - E_D}{kT}\right)}, \quad (73)$$

where $g_{D,\text{MC}}(T)$ is here called the effective degeneracy factor for donors given by

$$g_{D,\text{MC}}(T) = 2 \left[1 + \sum_{r=2}^l g_r \exp\left(-\frac{E_{r,D} - E_D}{kT}\right) \right] \exp\left(-\frac{\overline{E_{\text{ex},D}(T)}}{kT}\right). \quad (74)$$

4.3.3. The Hydrogenic Donor Case

A neutral donor can be approximately described as a hydrogen atom, that is, a positively ionized donor with an electron in orbit about the ionized donor. In this case, $E_{r,D}$ is given by [27, 28]

$$E_{r,D} = E_C - \frac{q^4 m_e^*}{8h^2 \epsilon_s^2 \epsilon_0^2 r^2} = E_C - \frac{\Delta E_{1,D}}{r^2} \quad (75)$$

and

$$\Delta E_{1,D} = 13.6 \frac{m_e^*}{m_0} \cdot \frac{1}{\epsilon_s^2} \quad (\text{eV}), \quad (76)$$

where m_0 is the free-space electron mass.

Because the Bohr radius (a^*) of the ground state is very small, E_D is expressed as

$$E_D = E_{1,D} - E_{\text{CCC}}, \quad (77)$$

where E_{CCC} is the central cell correction induced due to a strongly localized potential [26]. Therefore, the ground-state level does not obey the hydrogenic model. However, because the wave function extension of the $(r-1)$ th excited state is of the order $r^2 a^*$, the excited state levels are expected to follow the hydrogenic model.

4.3.4. Distribution Function for Acceptors

In the case of acceptors, different from those in the conduction band, there are two degenerate valence bands (i.e., a light-hole band and a heavy-hole band), indicating that there is an acceptor state for the light-hole band as well as an acceptor state for the heavy-hole band. When the density of electrons occupied at acceptors (n_A) is considered, therefore, $f_{MC}(E_A)$ is derived as [34, 35]

$$f_{MC}(E_A) \equiv \frac{n_A}{N_A} = \frac{1}{1 + g_{A,MC}(T) \exp\left(-\frac{E_F(T) - E_A}{kT}\right)}, \quad (78)$$

where $g_{A,MC}(T)$ is here called the effective degeneracy factor for acceptors given by

$$g_{A,MC}(T) = 4 \left[1 + \sum_{r=2}^l g_r \exp\left(-\frac{E_A - E_{r,A}}{kT}\right) \right] \exp\left(-\frac{\overline{E_{ex,A}(T)}}{kT}\right). \quad (79)$$

Here, $\overline{E_{ex,A}(T)}$ is the ensemble average of the ground and excited state levels of the acceptor, measured from E_A , and is given by

$$\overline{E_{ex,A}(T)} = \frac{\sum_{r=2}^l (E_A - E_{r,A}) g_r \exp\left(-\frac{E_A - E_{r,A}}{kT}\right)}{1 + \sum_{r=2}^l g_r \exp\left(-\frac{E_A - E_{r,A}}{kT}\right)}, \quad (80)$$

$E_{r,A}$ is the $(r - 1)$ th excited state level of the acceptor, expressed as

$$E_{r,A} = E_V + \frac{q^4 m_h^*}{8h^2 \epsilon_s^2 \epsilon_0^2 r^2} = E_V + \frac{\Delta E_{1,A}}{r^2}, \quad (81)$$

and

$$\Delta E_{1,A} = 13.6 \frac{m_h^*}{m_0} \cdot \frac{1}{\epsilon_s^2} \text{ (eV)}. \quad (82)$$

The average acceptor level $\overline{E_A}(T)$ and the acceptor level are expressed as

$$\overline{E_A}(T) = E_A - \overline{E_{ex,A}(T)} \quad (83)$$

and

$$E_A = E_{1,A} + E_{CCC}. \quad (84)$$

4.3.5. Distribution Function Derived from Grand Canonical Ensemble

The grand canonical ensemble is an ensemble of the same subsystems, and particles can transfer from one subsystem into another subsystem, indicating that the number of particles in the subsystem (N) can change. The partition function (Ξ) for the grand canonical ensemble is given by [36]

$$\Xi = \sum_N z^N Z_N, \quad (85)$$

where

$$z = \exp\left(\frac{E_F(T)}{kT}\right), \quad (86)$$

Z_N is the partition function for the canonical ensemble for a given N , which is expressed as

$$Z_N = \sum \exp\left(-\frac{\sum_j n_j E_j}{kT}\right). \quad (87)$$

This summation is carried out over all the sets of $\{n_j\}$ under the condition

$$N = \sum_j n_j, \quad (88)$$

where E_j and n_j are the energy level and number of electrons at a j th state in the subsystem, respectively.

A donor is a subsystem. Each donor has one electron or no electron (i.e., $N = 0$ or 1). The electron is located at one state for the ground and excited states (i.e., $n_j = 0$ or 1). Moreover, the number of the spin's states and degenerate excited states should be taken into account. Therefore,

$$Z_0 = 1 \quad (89)$$

and

$$Z_1 = 2 \left[\exp\left(-\frac{E_D}{kT}\right) + \sum_{r=2}^l g_r \exp\left(-\frac{E_{r,D}}{kT}\right) \right]. \quad (90)$$

Finally,

$$\begin{aligned} \Xi &= \sum_{N=0}^1 z^N Z_N = Z_0 + z Z_1 \\ &= 1 + 2 \left[\exp\left(-\frac{E_D - E_F(T)}{kT}\right) + \sum_{r=2}^l g_r \exp\left(-\frac{E_{r,D} - E_F(T)}{kT}\right) \right]. \end{aligned} \quad (91)$$

The mean number $\langle N \rangle$ of electrons in the subsystem in thermal equilibrium is given by

$$\langle N \rangle = \frac{\sum_{N=0}^1 N z^N Z_N}{\Xi}. \quad (92)$$

Therefore, the distribution function including the influence of the excited states for a donor is derived as

$$f_{GC}(E_D) \equiv \langle N \rangle = \frac{1}{1 + \frac{1}{g_{D,GC}(T)} \exp\left(-\frac{E_F(T) - E_D}{kT}\right)}, \quad (93)$$

where

$$g_{D,GC}(T) = 2 \left[1 + \sum_{r=2}^l g_r \exp\left(-\frac{E_{r,D} - E_D}{kT}\right) \right], \quad (94)$$

which coincides with the reported distribution functions [27, 29, 31]. On the other hand, the distribution function for acceptors is derived as

$$f_{GC}(E_A) = \frac{1}{1 + g_{A,GC}(T) \exp\left(-\frac{E_F(T) - E_A}{kT}\right)}, \quad (95)$$

where

$$g_{A,GC}(T) = 4 \left[1 + \sum_{r=2}^l g_r \exp\left(-\frac{E_A - E_{r,A}}{kT}\right) \right]. \quad (96)$$

4.3.6. Comparison between Three Distribution Functions

If the influence of the excited states for a donor or an acceptor could be ignored (i.e., $l = 1$), $f_{MC}(E_D)$ or $f_{MC}(E_A)$ would coincide with $f_{FD}(E_D)$ or $f_{FD}(E_A)$.

The reason why $f_{GC}(E_D)$ is different from $f_{MC}(E_D)$ is discussed later. Because an electron can be at a higher excited state level at elevated temperatures, the energy of an electron bound to a donor increases with increasing T . Therefore, the average donor level should increase with T , which is consistent with Eqs. (71) and (72).

If, on the other hand, electrons were located at the ground-state level at all temperatures, Eq. (70) could be replaced by

$$E_{\text{total}} = E_D \cdot n_D + \sum_i E_i \cdot n(E_i) = \text{const.} \quad (97)$$

In this case, the distribution function for donors derived from the microcanonical ensemble viewpoint would coincide with $f_{GC}(E_D)$. This suggests that $f_{GC}(E_D)$ is correct only under the assumption that all the electrons bound to donors have E_D at all temperatures. In the same way as illustrated for $f_{GC}(E_D)$, if $\overline{E_A(T)}$ could be assumed to be E_A (i.e., $\overline{E_{\text{ex},A}(T)} = 0$), $f_{MC}(E_A)$ would coincide with $f_{GC}(E_A)$.

4.4. Determination of Reliable Density and Energy Level of Deep Dopant

By FCCS using $f_{MC}(E_A)$, in B-doped diamond, N_A , E_A , and N_D were determined to be $2.82 \times 10^{17} \text{ cm}^{-3}$, $E_V + 0.323 \text{ eV}$, and $1.95 \times 10^{16} \text{ cm}^{-3}$, respectively. The highest excited state considered here was the sixth excited state (i.e., $l = 7$), under which the best curve fitting was achieved. Because the radius of the sixth excited state is approximately 15 nm and the lattice constant for diamond is 0.356 nm, the number of C atoms in a sphere of radius 15 nm is approximately 2×10^6 . Because the C density is $1.8 \times 10^{23} \text{ cm}^{-3}$ and the C_B is approximately $2 \times 10^{17} \text{ cm}^{-3}$, there is on the other hand, one B atom in approximately 10^6 C atoms. These suggest that the condition (i.e., $l = 7$) is not so bad.

N_A , E_A , and N_D determined by FCCS using $f_{GC}(E_A)$ are also shown in Table 4. In Table 4, all the E_A values determined using three distribution functions seems reasonable. However, N_A for $f_{GC}(E_A)$ is highest, while N_A for $f_{MC}(E_A)$ is lowest. The N_A obtained using $f_{MC}(E_A)$ is closest to C_B . Therefore, $f_{MC}(E_A)$ is suitable for determining N_A from $p(T)$.

Table 4 shows N_A , E_A , and N_{comp} for the others determined by FCCS using $f_{\text{MC}}(E_A)$ or $f_{\text{GC}}(E_A)$. As is clear from Table 4, only $f_{\text{MC}}(E_A)$ led to reliable N_A , E_A , and N_D for heavily-doped cases.

In Te-doped $\text{Al}_{0.6}\text{Ga}_{0.4}\text{Sb}$ where $E_F(T)$ was shallower than the donor energy level, moreover, f_{MC} is suitable for determining the density and energy level of the Te donor from the temperature dependence of the electron concentration [19].

Judging from the previous discussions, the distribution function derived from the microcanonical ensemble viewpoint is most appropriate. The reason why a reasonable dopant density can be obtained using Eq. (73) or (78) is discussed from the viewpoint of the effective degeneracy factors. Figure 15 shows $g_{A,\text{FD}}$, $g_{A,\text{MC}}(T)$, and $g_{A,\text{GC}}(T)$ for 6H-SiC,

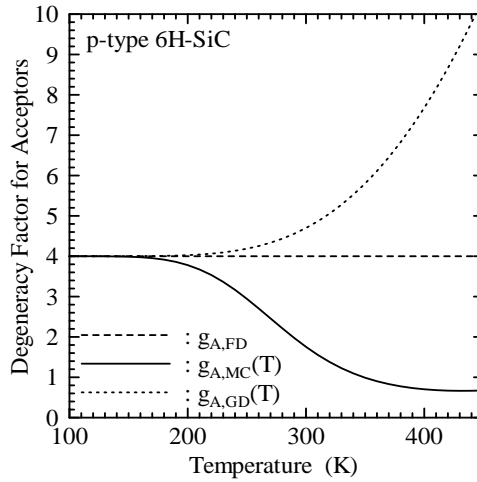


Figure 15. Temperature dependencies of simulated degeneracy factors for acceptors for 6H-SiC.

denoted by broken, solid, and dotted lines, respectively. $g_{A,\text{MC}}(T)$ decreases from 4 with increasing T , whereas $g_{A,\text{GC}}(T)$ increases. As the effective degeneracy factor for acceptors decreases, the distribution function for acceptors approaches 1 at the same T , indicating that in the case of $f_{\text{MC}}(E_A)$, the ionization efficiency of acceptors is highest at elevated temperatures.

Figure 16(a) depicts the ionized acceptor densities $N_A^-(T)$ simulated using N_A of $3.0 \times 10^{18} \text{ cm}^{-3}$, E_A of $E_V + 0.18 \text{ eV}$, N_D of $9.7 \times 10^{16} \text{ cm}^{-3}$, and the effective degeneracy factors for acceptors shown in Fig. 15, for $f_{\text{FD}}(E_A)$, $f_{\text{MC}}(E_A)$, and $f_{\text{GC}}(E_A)$, denoted by broken, solid, and dotted lines, respectively. As is clear from the figure, $N_A^-(T)$ for $f_{\text{MC}}(E_A)$ is highest at elevated temperatures. In the case of $f_{\text{MC}}(E_A)$, therefore, N_A required to satisfy the experimentally obtained $p(T)$ is much less than that determined using $f_{\text{FD}}(E_A)$ or $f_{\text{GC}}(E_A)$.

Another interpretation of Fig. 16(a) is as follows. As the temperature increases, the possibility increases that a hole bound to the acceptor is located at a higher excited state level. That is why the acceptor can more easily emit a hole to the valence band at elevated temperatures. This coincides with Eq. (83). Therefore, it is clear that the excited states of

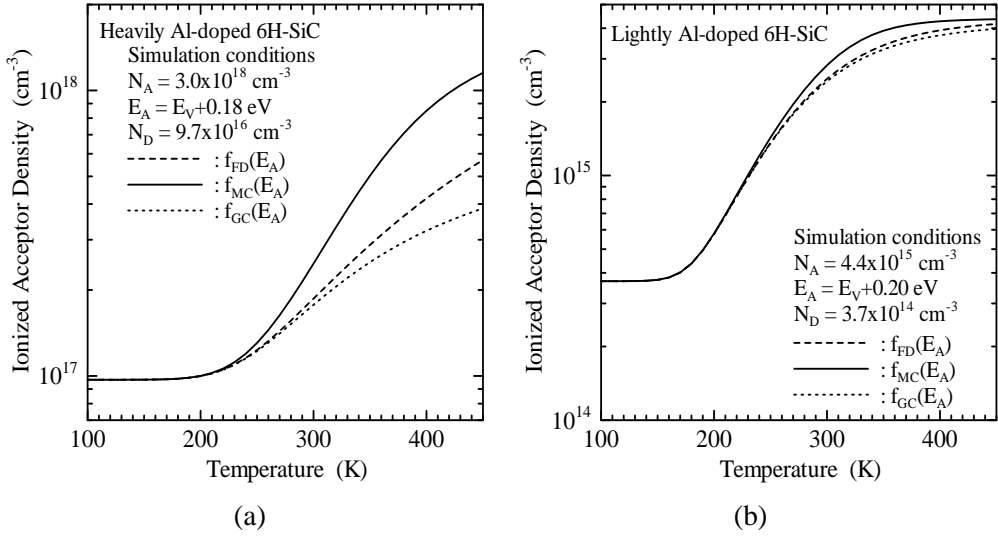


Figure 16. Temperature dependencies of simulated ionized acceptor densities; (a) for heavily Al doped 6H-SiC and (b) for lightly Al doped 6H-SiC.

the acceptor enhance the ionization of the acceptor at elevated temperatures.

Figure 16(b) shows $N_A^-(T)$ simulations for the lightly Al-doped 6H-SiC using the effective degeneracy factors for acceptors shown Fig. 15. Here, N_A , E_A , and N_D used in the simulation were $4.4 \times 10^{15} \text{ cm}^{-3}$, $E_V + 0.20 \text{ eV}$, and $3.7 \times 10^{14} \text{ cm}^{-3}$, respectively. In the figure, the broken, solid, and dotted lines represent the $N_A^-(T)$ simulations for $f_{FD}(E_A)$, $f_{MC}(E_A)$, and $f_{GC}(E_A)$, respectively. Although the effective degeneracy factors for acceptors in the lightly-doped case are the same as those in the heavily-doped case, $N_A^-(T)$ for $f_{FD}(E_A)$, $f_{MC}(E_A)$, and $f_{GC}(E_A)$ are similar to each other in the lightly-doped case. This is because the effective degeneracy factor for acceptors has little effect on $f_{FD}(E_A)$, $f_{MC}(E_A)$, and $f_{GC}(E_A)$, when $E_F(T)$ is far from the acceptor level. To determine N_A from $p(T)$, therefore, $f_{MC}(E_A)$ is the most appropriate among them.

5. Transient Capacitance Method for High-Resistivity Semiconductors

5.1. Dependence of Diode Capacitance on Measurement Frequency

Let us consider the capacitance of a Schottky barrier diode measured at different frequencies. Figure 17(a) and (b) show the energy band diagram and the equivalent circuit of the Schottky barrier diode, respectively. At low frequency ($f \ll 1/2\pi\epsilon_s\epsilon_0\rho$) that is a normal measurement frequency, the equivalent circuit is described as Fig. 17(c), insisting that the capacitance measured is due to the depletion width of the diode.

At high frequency ($f \gg 1/2\pi\epsilon_s\epsilon_0\rho$), on the other hand, the capacitance measured is the geometric capacitance calculated using the semiconductor thickness, because the equivalent circuit can be expressed as Fig. 17(d).

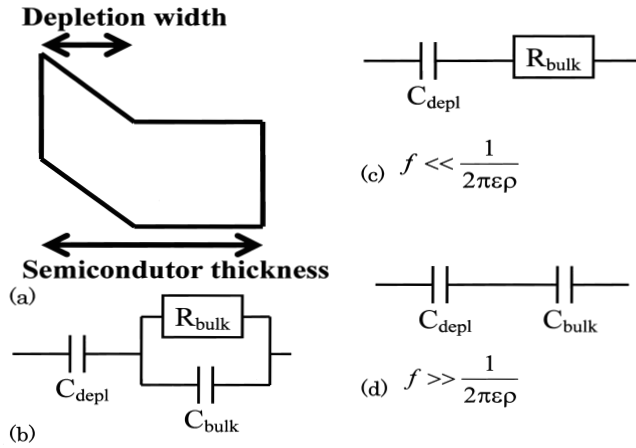


Figure 17. Capacitance measurements for Schottky barrier diode; (a) energy band diagram, (b) equivalent circuit of the diode, (c) equivalent circuit at low measurement frequency, and (d) equivalent circuit at high measurement frequency. Here, ϵ is the permittivity for semiconductor ($\epsilon_s \epsilon_0$).

5.2. Capacitance-Voltage Characteristics

Capacitance–voltage (C – V) and transient capacitance $C(t)$ measurements were carried out in a Schottky barrier diode fabricated using 0.3-mm-thick high-resistivity p-type 6H-SiC at a frequency of 1 MHz in the temperature range between 300 and 600 K, where the electrode area was 3.14 mm² [37].

The capacitance of the diode at 300 K was independent of reverse bias as shown by ■ in Fig. 18(a), and was close to the geometric capacitance calculated using the thickness of the 6H-SiC substrate. The ○ in Fig. 18(a) represents the C – V characteristics at 500 K. At ≥ 450 K, the capacitance was dependent on reverse bias, indicating that the measured capacitance is determined by the width of the depletion region. Therefore, the capacitance was measured at ≥ 450 K. Figure 18(b) shows the C^{-2} – V characteristics of the diode at 500 K. From the slope, the value of N_A was estimated as 9.3×10^{14} cm^{−3}, where N_A includes the acceptor density and hole-trap densities.

5.3. Transient Capacitance

The $C(t)$ was measured after an applied voltage was step-functionally changed from 0 to a reverse bias (V_R) of −20 V. Figure 19 shows the $C(t)$ and ICTS signal $S(t)$ of the diode at 500 K, indicated by broken and solid lines, respectively, where

$$S(t) \equiv t \frac{dC(t)^2}{dt}. \quad (98)$$

From the number of peaks of $S(t)$ in Fig. 19, at least three types of hole-trap species could be detected. These hole traps are here referred to as HRH2, HRH3, and HRH4, as shown in Fig. 19. Judging from the ICTS signals in the shorter or longer time range, there are at least

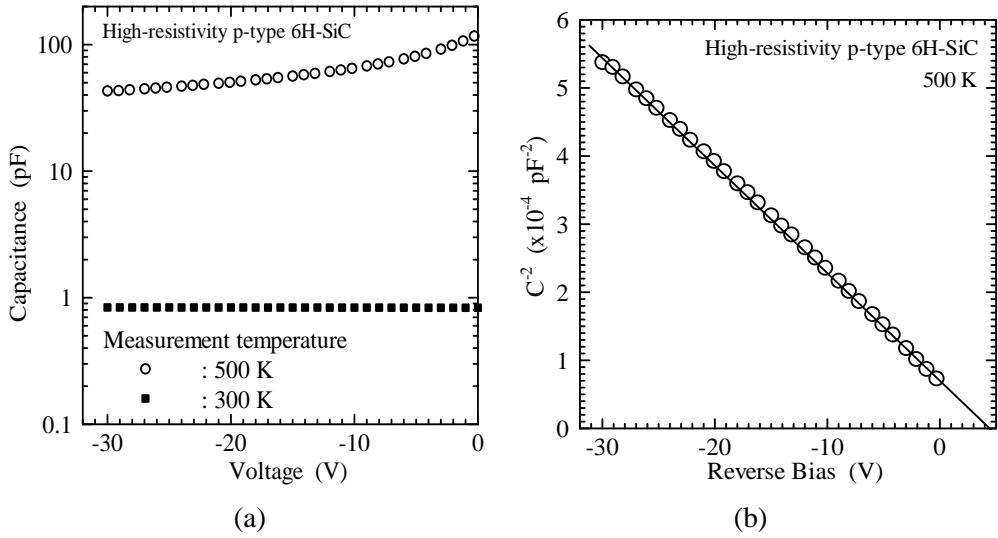


Figure 18. Characteristics of diode; (a) C - V characteristics at 300 K and 500 K and (b) $1/C^{-2}$ - V characteristics at 500 K.

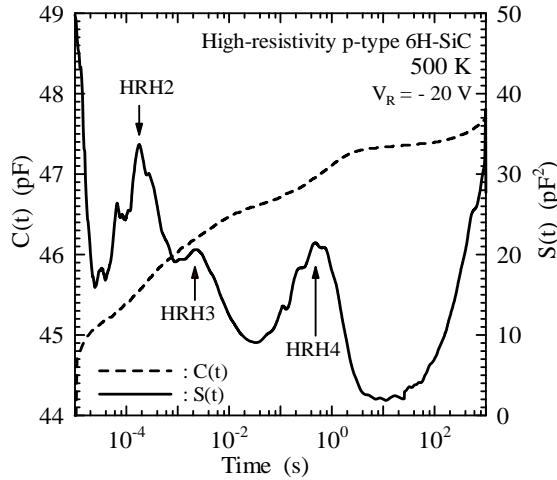


Figure 19. Transient capacitance and ICTS signal at 500 K.

another two unresolved hole traps. Figure 20(a) and (b) show the ICTS signal at 470 and 530 K, respectively, in which these two contributions could be fully resolved and labeled HRH1 and HRH5, respectively. Finally, five types of hole traps could be observed in the temperature range between 450 and 600 K.

The ICTS signal is theoretically expressed as [8]

$$S(t) = \frac{q\epsilon_s\epsilon_0 A^2}{2(V_D - V_R)} \sum_i N_{\text{TH}i} e_{\text{TH}i} t \exp(-e_{\text{TH}i} t), \quad (99)$$

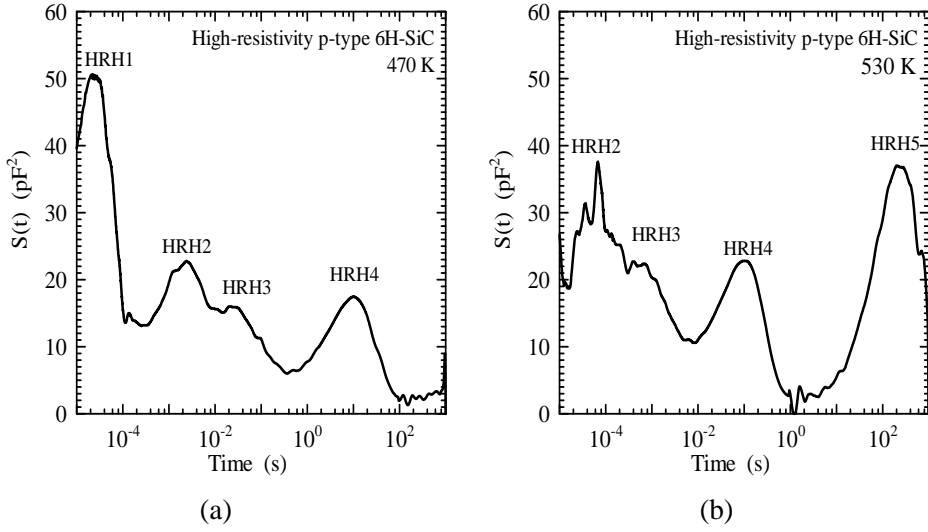


Figure 20. ICTS signal at 470 K (a) and at 530 K (b).

which has a peak at

$$t_{\text{peak}i} = \frac{1}{e_{\text{TH}i}}, \quad (100)$$

where V_D is the diffusion potential of the diode, and $e_{\text{TH}i}$ is the emission rate of an i th hole trap, respectively. Moreover, $N_{\text{TH}i}$ is given as [8]

$$N_{\text{TH}i} = \frac{2(V_D - V_R)}{q\epsilon_s\epsilon_0 A^2} S(t_{\text{peak}i}) \exp 1. \quad (101)$$

On the other hand, the hole concentration at the i th trap ($p_{\text{TH}i}$) varies as

$$\frac{dp_{\text{TH}i}}{dt} = \sigma_{\text{TH}i} v_{\text{th}} p (N_{\text{TH}i} - p_{\text{TH}i}) - e_{\text{TH}i} p_{\text{TH}i}, \quad (102)$$

where

$$p_{\text{TH}i} = N_{\text{TH}i} [1 - f(E_{\text{TH}i})], \quad (103)$$

$f(E_{\text{TH}i})$ is the electron occupation probability for the i th hole trap, given as

$$f(E_{\text{TH}i}) = \frac{1}{1 + g_{\text{TH}i} \exp\left(\frac{E_{\text{TH}i} - E_F}{kT}\right)}, \quad (104)$$

p is the hole concentration, v_{th} is the thermal velocity of electron, and $\sigma_{\text{TH}i}$ and $g_{\text{TH}i}$ are the cross section and degeneracy factor of the i th hole trap, respectively. In thermal equilibrium ($dp_{\text{TH}i}/dt = 0$), $e_{\text{TH}i}$ is derived using Eqs. (102)-(104) as

$$e_{\text{TH}i} = \nu_{\text{TH}i} \exp\left(-\frac{E_{\text{TH}i} - E_V}{kT}\right) \quad (105)$$

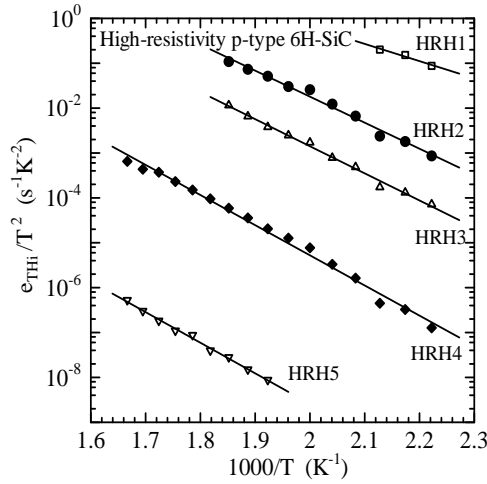


Figure 21. Relationship between e_{THi}/T^2 and $1/T$.

Table 5. Densities, energy levels and cross sections of hole traps in high-resistivity 6H-SiC determined by ICTS.

Hole-trap species	Density (cm^{-3})	Energy level (eV)	Cross section (cm^2)
HRH1	5.0×10^{13}	$E_V + 0.76$	1×10^{-14}
HRH2	3.3×10^{13}	$E_V + 1.15$	2×10^{-12}
HRH3	2.0×10^{13}	$E_V + 1.20$	5×10^{-13}
HRH4	2.1×10^{13}	$E_V + 1.33$	4×10^{-14}
HRH5	3.6×10^{13}	$E_V + 1.35$	4×10^{-17}

and

$$\nu_{THi} = \frac{N_V \sigma_{THi} v_{th}}{g_{THi}}. \quad (106)$$

Since N_V is proportional to $T^{1/2}$ and v_{th} is proportional to $T^{3/2}$, ν_{THi} is expressed as

$$\nu_{THi} = B_i \sigma_{THi} T^2 \quad (107)$$

and

$$B_i = \frac{4\pi\sqrt{6\pi}m_h^*k^2}{g_{THi}h^3}. \quad (108)$$

The relationship between e_{THi}/T^2 and $1/T$ is shown in Fig. 21. In Fig. 21, the optimum straight line fitting to experimental data for each trap could be obtained, from which the values of E_{THi} and σ_{THi} could be determined and listed in Table 5. Here, m_h^* and g_{THi} were assumed to be m_0 and 1, respectively. This table also includes N_{Ti} estimated using Eq. (101), which is averaged over the temperature range of the measurement. The sum of the densities of intrinsic defects detected is $1.6 \times 10^{14} \text{ cm}^{-3}$, whereas the sum of the

acceptor density and hole-trap densities is approximately $9 \times 10^{14} \text{ cm}^{-3}$. Therefore, the intrinsic defects strongly decrease the majority-carrier concentration in the high-purity 6H-SiC, which makes ρ as high as approximately $10^6 \Omega \text{ cm}$.

6. Heterojunction-Monitored Capacitance Method for Amorphous Semiconductors

6.1. Steady-State HMC

The optoelectronic properties of high-resistivity amorphous semiconductors such as undoped hydrogenated amorphous silicon (a-Si:H) are critically linked with the density-of-state (DOS) distribution, $g(E)$, in the mobility gap. Measurement of $g(E)$ and an understanding of the nature of the gap states are, therefore, very important. However, DLTS and ICTS are not feasible to determine the $g(E)$ using a Schottky barrier diode fabricated from high-resistivity amorphous semiconductor, because it is impossible to measure the depletion width of the junction.

In order to measure the depletion width in high-resistivity amorphous semiconductors, an amorphous semiconductor/crystalline semiconductor heterojunction is discussed. The method to determine $g(E)$ in amorphous semiconductors using heterojunctions is referred to as heterojunction-monitored capacitance (HMC) methods [38, 39, 40, 41, 42]. Since the conduction type of undoped a-Si:H is n-type, for example, p-type crystalline Si (c-Si) is selected. Figure 22(a), (b), (c), and (d) show the energy-band diagram, potential, charges in statics, and charges corresponding to AC voltage in the p-type c-Si/undoped a-Si:H/Mg heterojunction, respectively, where Mg forms an ohmic contact with the undoped a-Si:H [38, 43]. In the figure, the gap states as indicated by the black area of (a) are positively charged states, and \ominus represents negatively charged acceptors in the depletion region of p-type c-Si.

The depletion region formed by the heterojunction is considered. When a bias voltage (V) is applied, it produces space-charge layers both in a-Si:H and c-Si. Since this p-type c-Si has only shallow acceptors, the space charge in the c-Si is formed by negatively charged acceptors. However, localized states in a-Si:H distribute within the gap.

Let us discuss the origin of the positive space charge in a-Si:H using Fig. 22. In the neutral region, all the gap states below E_F are occupied by electrons, whereas in the depletion region, the gap states above E_{OB2} are devoid of electrons, where E_{OB2} is determined from the condition that the thermal emission rate for electrons is equal to that for holes and given by [39]

$$E_{OB2} = E_V + E_{g2} + \frac{kT}{2} \ln \left(\frac{\nu_h}{\nu_e} \right), \quad (109)$$

where ν_h and ν_e are the attempt-to-escape frequencies for holes and electrons, respectively. Therefore, the gap states in the area painted in black in Fig. 22(a) behave like positive space charges (herein referred to as donor-like states). The density of the donor-like states is constant in the spatial position between 0 and the depletion width in a-Si:H (W_2). This, together with the density of donors (if they exist), gives the effective density of the donor-like states (N_I), as shown in Fig. 22(c). Figure 22(b) shows the potential variation with

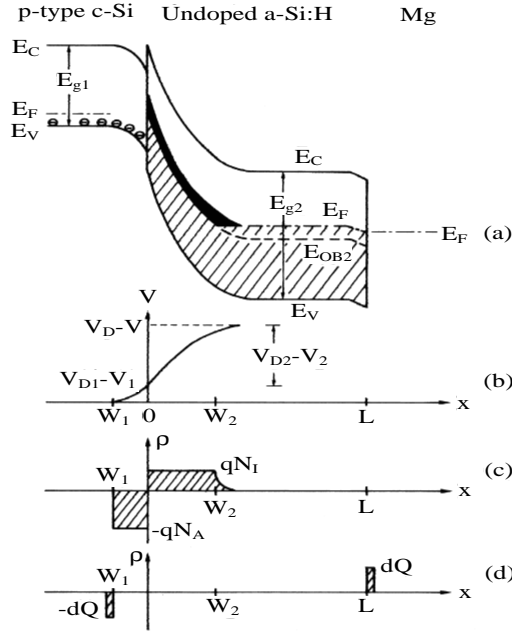


Figure 22. Schematic sketches of undoped a-Si:H/p-type c-Si heterojunction; (a) energy-band diagram, (b) potential, (c) charges in statistic, and (d) charges corresponding to AC voltage.

distance. The depletion widths (W_1 and W_2) are given by

$$qN_A W_1 \cong qN_I W_2 \quad (110)$$

with

$$W_1 = \sqrt{\frac{2\epsilon_{s1}\epsilon_0 (V_{D1} - V_1)}{qN_A}} \quad (111)$$

and

$$W_2 \cong \sqrt{\frac{2\epsilon_{s2}\epsilon_0 (V_{D2} - V_2)}{qN_I}}. \quad (112)$$

Here, E_g is the bandgap and L is the thickness of a-Si:H. The subscripts 1 and 2 refer to c-Si and a-Si:H, respectively.

The capacitance is measured with a small AC voltage at 1 MHz. The resistivity (ρ_1) of c-Si is about $1 \Omega\cdot\text{cm}$ so that the dielectric relaxation time ($\epsilon_{s1}\epsilon_0\rho_1$) becomes 10^{-12} s, indicating that the capacitance C_1 in c-Si is given by

$$C_1 = \frac{\epsilon_{s1}\epsilon_0 A}{W_1}. \quad (113)$$

On the other hand, the resistivity (ρ_2) of undoped a-Si:H is about $10^9 \Omega\text{cm}$. Then, the dielectric time ($\epsilon_{s2}\epsilon_0\rho_2$) becomes 10^{-3} s, suggesting that at 1 MHz AC voltage the capaci-

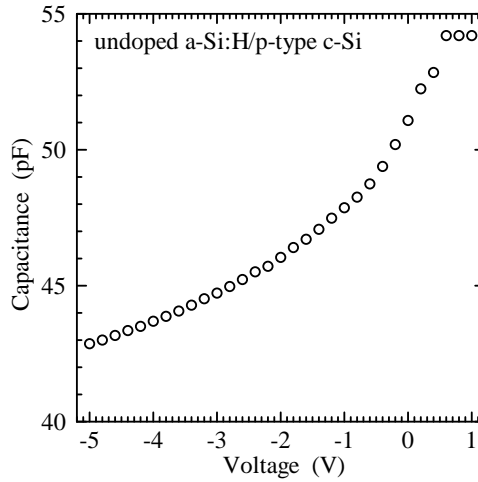


Figure 23. $C - V$ characteristics of undoped a-Si:H/p-type c-Si heterojunction at 1 MHz.

tance C_2 in a-Si:H can simply be given by

$$C_2 = \frac{\epsilon_{s2}\epsilon_0 A}{L}. \quad (114)$$

The measured capacitance C at 1 MHz is expressed as

$$\frac{1}{C} = \frac{1}{C_1} + \frac{1}{C_2}, \quad (115)$$

because the redistribution of charge (dQ) can spatially respond to the 1 MHz AC voltage at W_1 and L , shown in Fig. 22(d). From Eqs. (110)-(112), the following equation is obtained:

$$\frac{V_{D1} - V_1}{V_{D2} - V_2} \cong \frac{N_I \epsilon_{s2}}{N_A \epsilon_{s1}}. \quad (116)$$

Finally, the next equation is derived from Eqs. (111), (113), (115), and (116):

$$\begin{aligned} W_1^2 &= \left[\epsilon_{s1} \epsilon_0 A \left(\frac{1}{C} - \frac{1}{C_2} \right) \right]^2 \\ &\cong \frac{2\epsilon_{s1}\epsilon_{s2}\epsilon_0 N_I (V_D - V)}{q N_A (N_A \epsilon_{s1} + N_I \epsilon_{s2})}. \end{aligned} \quad (117)$$

From the $W_1^2 - V$ characteristics, therefore, N_I can be estimated.

Figure 23 shows the high-frequency $C - V$ characteristics of an undoped a-Si:H/p-type c-Si heterojunction. The value of N_A , L , and A are $1.0 \times 10^{16} \text{ cm}^{-3}$, approximately $1.5 \mu\text{m}$, and 0.785 mm^2 , respectively. Because W_1 is close to 0 at forward biases, the saturated value of 54.2 pF is determined by the thickness of a-Si:H.

Figure 24(a) shows the $C^{-2} - V$ characteristics, and the straight relationship could not be obtained. Figure 24(b) shows the $W_1^2 - V$ characteristics, where $C_2 = 54.2 \text{ pF}$. Since the

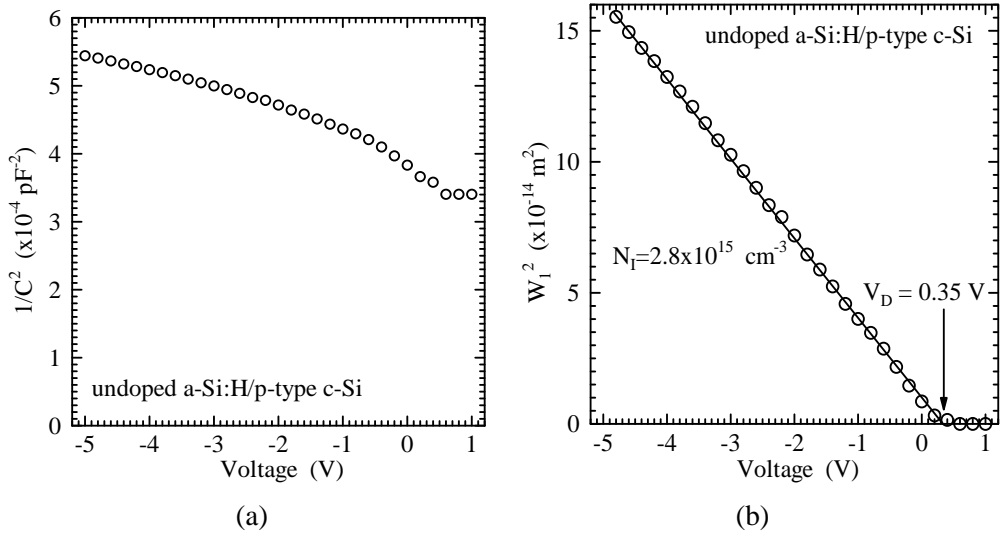


Figure 24. Characteristics of undoped a-Si:H/p-type c-Si heterojunction; (a) $C^{-2} - V$ characteristics and (b) $W_1^2 - V$ characteristics.

data reveal a good linear relationship, N_I and V_D were determined to be $2.8 \times 10^{15} \text{ cm}^{-3}$ and 0.35 V, respectively. The value of W_2 at -5 V is calculated to be approximately $1.4 \text{ } \mu\text{m}$ using Eq. (112), indicating that $W_2 < L$. It is noted that W_2 at the maximum reverse bias should be shorter than L .

6.2. Heterojunction-Monitored Capacitance Spectroscopy

In order to determine $g(E)$, the transient HMC is considered after V_R is applied to the diode over the zero-bias condition, as shown in Fig. 25. In energy-band diagrams, the gap states as indicated by the hatched area are neutral, and in the depletion region the empty gap states between E_F and E_{OB2} behave like positively charged states. This method is referred to as heterojunction-monitored capacitance spectroscopy (HMCS) [39, 41, 42].

Figure 25(a) shows the energy-band diagram and space-charge density at $t < 0$. At $t = 0$, V_R is applied across the whole of the amorphous and crystalline components. After the reverse bias has been on for $\epsilon_{s2}\epsilon_0\rho_2$, the space charge in the vicinity of the heterojunction will redistribute itself in response to the applied potential, as shown in Fig. 25(b). The transient HMC $C_{HM}(t)$ after $\epsilon_{s2}\epsilon_0\rho_2$ can be analyzed from Eq. (117), and N_I at t can be expressed as

$$N_I(t) = \frac{\epsilon_{s1}V_c(t)N_A}{\epsilon_{s2}[V_D - V_R - V_c(t)]}, \quad (118)$$

with

$$V_c(t) = \frac{qN_AW_1^2(t)}{2\epsilon_{s1}\epsilon_0} \quad (119)$$

and

$$W_1(t) = \epsilon_{s1}\epsilon_0A \left[\frac{1}{C_{HM}(t)} - \frac{1}{C_2} \right], \quad (120)$$

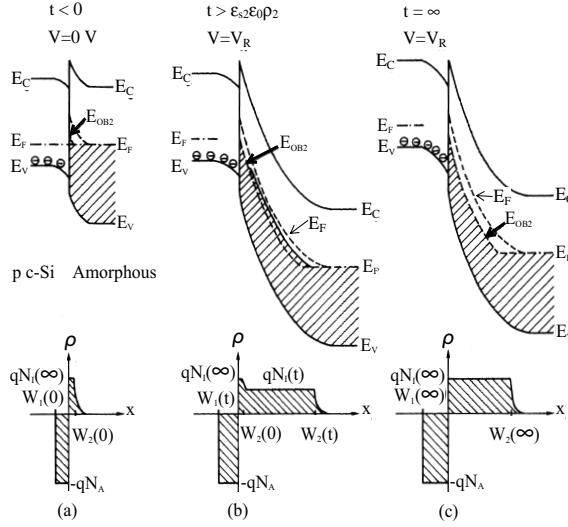


Figure 25. Schematic sketches (energy-band diagram and space-charges density) of undoped a-Si:H/p-type c-Si heterojunction at three different times; (a) $t < 0$, (b) $t > \epsilon_{s2}\epsilon_0\rho_2$, and (c) $t = \infty$.

where $W_1(t)$ is the depletion width at t and $V_c(t)$ is the voltage across the depletion region of c-Si at t . To make this analysis feasible, the absolute value of V_R has to be necessarily much higher than V_D , so that the relationship of $N_I W_2(t) \gg N_I W_2(0)$ is valid and the average value of N_I over the depletion region at t is close to $N_I(t)$. This condition also suggests that interface states do not affect the measurement of HMC.

The function $H(t)$ is defined as

$$H(t) \equiv t \left(\frac{dN_I(t)}{dt} \right). \quad (121)$$

On the other hand, $H(t)$ is theoretically derived as

$$\begin{aligned} H(t) &= \int_{E_V}^{E_C} \left[f_{FD}(E') - F_{\infty}(E') \right] g(E') \left[e_e(E') + e_h(E')t \right] \\ &\quad \times \exp \left\{ - \left[e_e(E') + e_h(E') \right] t \right\} dE' \end{aligned} \quad (122)$$

with

$$f_{FD}(E) = \frac{1}{1 + \exp \left(\frac{E - E_F}{kT} \right)}, \quad (123)$$

$$F_{\infty}(E) = \frac{e_h(E)}{e_e(E) + e_h(E)}, \quad (124)$$

$$e_e(E) = \nu_e \exp \left(- \frac{E_C - E}{kT} \right), \quad (125)$$

and

$$e_h(E) = \nu_h \exp \left(-\frac{E - E_V}{kT} \right). \quad (126)$$

Under the conditions that $e_e(E) \gg e_h(E)$ and $f_{FD}(E) \sim 1$ (i.e., for the gap states between E_F and E_{OB2}), Eq. (122) can be approximately expressed as

$$H(t) \cong \int_{E_V}^{E_C} g(E') e_e(E') t \exp \left[-e_e(E') t \right] dE'. \quad (127)$$

Assuming that the function of $e_e(E') t \exp[-e_e(E') t]$ behaves as a delta function, $kT \delta(E - E')$, since the integrated value of $e_e(E') t \exp[-e_e(E') t]$ from $E = 0$ to ∞ using Eq. (125) is kT , we can easily derive the following relationship from Eq. (127):

$$g[E(t)] \cong \frac{H(t)}{kT} \quad (128)$$

and

$$E_C - E(t) = kT \ln(\nu_e t). \quad (129)$$

Using $g(E)$ calculated from Eq. (128) as an initial $g(E)$, we can determine $g(E)$ from which $H(t)$ of Eq. (122) can be obtained to fit the measured $H(t)$.

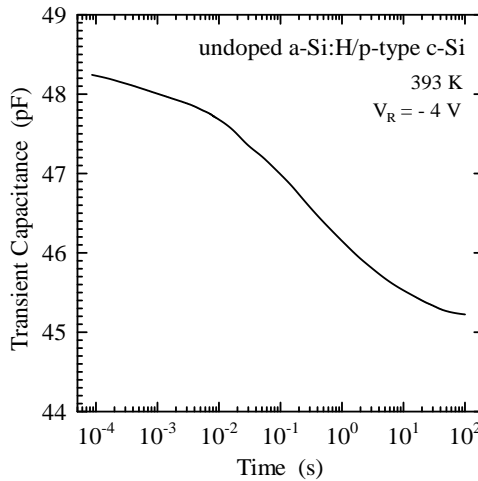


Figure 26. Transient capacitance of undoped a-Si:H/p-type c-Si heterojunction.

Figure 26 shows the change in the capacitance of the heterojunction after V_R of -4 V is applied to the diode under the zero-bias condition.

The solid line in Fig. 27 represents $g(E)$ for a-Si:H calculated using $C_{HM}(t)$ in Fig 26, when $\nu_e = 10^{13} \text{ s}^{-1}$. Here, the value of ν_e can be estimated from the temperature dependence of $H(t)$ [39, 42]. In Fig. 27, the broken and dashed-dotted lines represent $g(E)$ for a-Si_{1-x}Ge_x:H and a-Si_{1-x}C_x:H, respectively, where E_o is the optical bandgap of amorphous semiconductors.

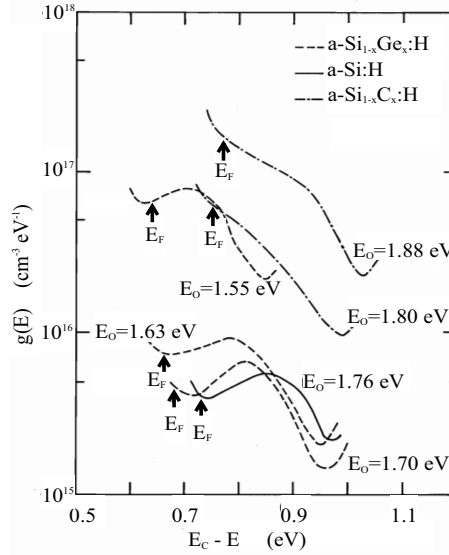


Figure 27. Density of states for a-Si:H, a-Si_{1-x}Ge_x:H, and a-Si_{1-x}C_x:H.

7. Discharge Current Transient Spectroscopy

7.1. Basic Concept

Even when the resistivities of materials are too high to measure the change of the depletion width in diodes by capacitance, it is able to measure the transient current in the diodes. Therefore, the transient current due to re-emission (or discharge) of charges from traps is considered.

In graphical peak analysis methods, it is desired that functions to be evaluated have a peak value (NS_{Ti}) at a peak discharge time ($t_{peaki} = 1/e_{Ti}$), where NS_{Ti} is the density per unit area of an i th trap, respectively. One of the functions that satisfy the condition mentioned earlier is expressed as

$$D(t) = \sum_{i=1} NS_{Ti} e_{Ti} t \exp(-e_{Ti} t + 1), \quad (130)$$

where t is the discharge time. Here, when traps are confirmed to be uniformly distributed in the direction of the film thickness, the density per unit volume can be calculated as NS_{Ti} over the film thickness.

When we can introduce a function in which each peak appears at

$$t_{peaki} = \frac{1}{e_{Ti} + e_{ref}}, \quad (131)$$

we can shift the peak discharge time to the measurement time range by changing the parameter (e_{ref}). This indicates that we can determine NS_{Ti} and e_{Ti} in a wide emission-rate

range, even when the measurement time range is limited. The function that satisfies this condition is

$$D(t, e_{\text{ref}}) = \sum_{i=1} NS_{Ti} e_{Ti} t \exp[-(e_{Ti} + e_{\text{ref}})t + 1]. \quad (132)$$

In this case, each peak value is

$$D(t_{\text{peak}i}, e_{\text{ref}}) = NS_{Ti} (1 - e_{\text{ref}} t_{\text{peak}i}), \quad (133)$$

at $t_{\text{peak}i}$ expressed as Eq. (131). Therefore, using $t_{\text{peak}i}$ and $D(t_{\text{peak}i}, e_{\text{ref}})$, the values of NS_{Ti} and e_{Ti} can be determined as

$$NS_{Ti} = \frac{D(t_{\text{peak}i}, e_{\text{ref}})}{1 - e_{\text{ref}} t_{\text{peak}i}} \quad (134)$$

and

$$e_{Ti} = \frac{1}{t_{\text{peak}i}} - e_{\text{ref}}, \quad (135)$$

respectively.

In order to obtain Eq. (132), we define the function to be evaluated as

$$D(t, e_{\text{ref}}) \equiv \frac{t}{qA} [I_{\text{dis}}(t) - I_{\text{ssl}}(V_{\text{dis}})] \exp(-e_{\text{ref}}t + 1), \quad (136)$$

where $I_{\text{ssl}}(V_{\text{dis}})$ is the steady-state leakage current at the discharge voltage (V_{dis}).

In the case of thermionic emission processes, ΔE_{Ti} can be determined from the temperature dependence of e_{Ti} , since e_{Ti} is given by

$$e_{Ti} = \nu_{Ti} \exp\left(-\frac{\Delta E_{Ti}}{kT}\right). \quad (137)$$

When the time dependence of the depolarization of an i th dipole in a dielectric film is given by

$$\exp\left(-\frac{t}{\tau_i}\right), \quad (138)$$

the polarization (P_i) and relaxation time (τ_i) of the i -th dipole can be determined using DCTS. In this case, e_{Ti} and NS_{Ti} in Eq. (132) should be replaced by $1/\tau_i$ and P_i/q , respectively.

7.2. Theoretical Consideration

A capacitor or a diode is considered. When a charge voltage (V_{cha}) is applied to the capacitor in the interval of $-t_{\text{cha}} < t < 0$, a charge current (I_{cha}), which fills traps with charged carriers (electrons or holes), flows through the capacitor. In the case of diodes, V_{cha} is usually 0 V. By $t = 0$, all the traps are assumed to capture charged carriers, indicating that at $t = 0$ the density per unit area, $NS_{Ti}(t)$, of charged carriers captured at the i th trap is expressed as

$$NS_{Ti}(0) = NS_{Ti}. \quad (139)$$

At $t = 0$, the applied voltage is changed from V_{cha} to V_{dis} . Since the resistance in the external measurement circuit is very low, the charge due to the geometric capacity disappears in a very short time. At $t > 0$, therefore, the measured $I_{\text{dis}}(t)$ arises due to the emission of charged carriers from traps as well as due to $I_{\text{ssl}}(V_{\text{dis}})$.

Since $NS_{\text{Ti}}(t)$ follows the rate equation

$$\frac{dNS_{\text{Ti}}(t)}{dt} = -NS_{\text{Ti}}(t)e_{\text{Ti}}, \quad (140)$$

the total charge, $Q(t)$, in the film is expressed as

$$\begin{aligned} Q(t) &= qA \sum_{i=1} NS_{\text{Ti}}(t) \\ &= qA \sum_{i=1} NS_{\text{Ti}} \exp(-e_{\text{Ti}}t). \end{aligned} \quad (141)$$

Because the decrease of $Q(t)$ results in the transient discharge current,

$$I_{\text{dis}}(t) = -\frac{dQ(t)}{dt} + I_{\text{ssl}}(V_{\text{dis}}). \quad (142)$$

From Eq. (136), $D(t, e_{\text{ref}})$ is theoretically expressed as

$$D(t, e_{\text{ref}}) = \sum_{i=1} NS_{\text{Ti}} e_{\text{Ti}} t \exp[-(e_{\text{Ti}} + e_{\text{ref}})t + 1]. \quad (143)$$

As is clear from Eq. (143), we have obtained a suitable function for the graphical peak analysis method. This analysis is referred to as discharge current transient spectroscopy (DCTS) [44, 45, 46, 47, 48], and can be carried out using software developed in-house (<http://www.osakac.ac.jp/labs/matsuura/>).

7.3. Shift of Peak Discharge Time to Measurement Time Range

It is demonstrated that e_{ref} in Eq. (136) is a useful parameter when the time range of the measurement is limited. Figure 28(a) shows the transient discharge current, which is simulated assuming the following two kinds of traps. NS_{T1} and e_{T1} for Trap1 are $1 \times 10^{12} \text{ cm}^{-2}$ and 0.5 s^{-1} , respectively, NS_{T2} and e_{T2} for Trap2 are $1 \times 10^{12} \text{ cm}^{-2}$ and 0.0005 s^{-1} , respectively, and A is 1 mm^2 .

Figure 28(b) shows the DCTS signals. The solid line represents the DCTS signal with $e_{\text{ref}} = 0 \text{ s}^{-1}$. In this case, only one peak is detected, and the peak discharge time and peak value are 2.00 s and $1.00 \times 10^{12} \text{ cm}^{-2}$, respectively. From Eqs. (134) and (135), NS_{T1} and e_{T1} are determined to be $1.00 \times 10^{12} \text{ cm}^{-2}$ and $5.00 \times 10^{-1} \text{ s}^{-1}$, respectively. Since the other peak is not detected when $e_{\text{ref}} = 0 \text{ s}^{-1}$, however, it is impossible to determine NS_{T2} and e_{T2} .

The broken line in Fig. 28(b) represents the DCTS signal with $e_{\text{ref}} = 0.001 \text{ s}^{-1}$. In this case, two peaks appear in the figure, and the two peak discharge times are 2.00 s and 667 s . Using Eqs. (134) and (135), therefore, NS_{T1} and e_{T1} of the trap corresponding to 2.00 s are determined to be $1.00 \times 10^{12} \text{ cm}^{-2}$ and $5.00 \times 10^{-1} \text{ s}^{-1}$, respectively, while

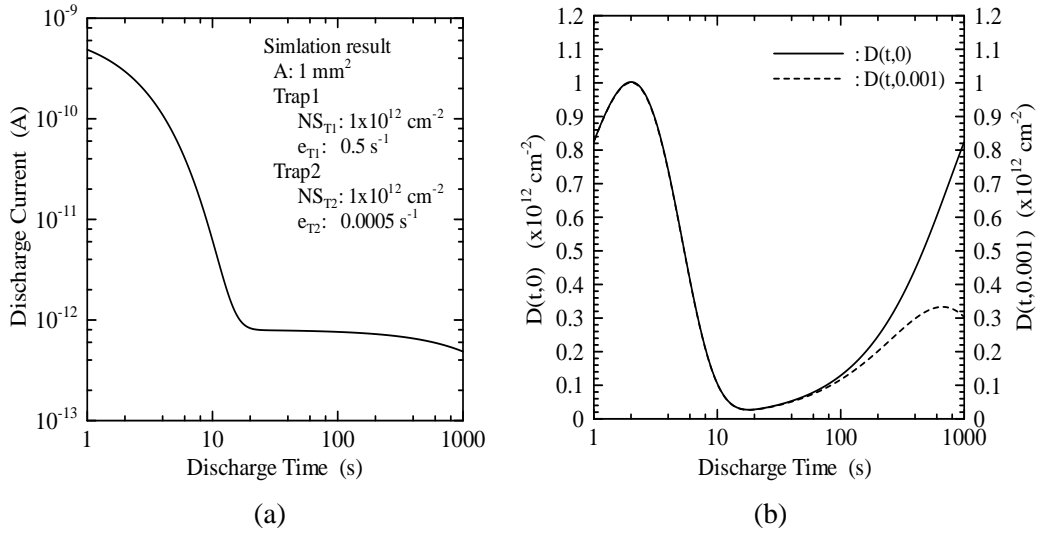


Figure 28. Simulated transient discharge current (a) and DCTS signals (b).

NS_{T2} and e_{T2} of the trap corresponding to 667 s are determined to be 1.00×10^{12} cm⁻² and 5.00×10^{-4} s⁻¹, respectively. The obtained values are in good agreement with the values using which the transient discharge current was simulated. This indicates that NS_{Ti} and e_{Ti} can be determined in a wide emission-rate range by changing e_{ref} , even when the measurement time range is limited.

7.4. Distinction among Traps with Close Emission Rates

It is demonstrated that e_{ref} in Eq. (136) is also useful when there are traps with close emission rates in the film. Figure 29 shows the transient discharge current, which is simulated assuming the following two kinds of traps. NS_{T1} and e_{T1} for Trap1 are 3×10^{12} cm⁻² and 0.05 s⁻¹, respectively, NS_{T2} and e_{T2} for Trap2 are 1×10^{12} cm⁻² and 0.01 s⁻¹, respectively, and A is 1 mm². In this case, e_{T2} is very close to e_{T1} .

The solid line in Fig. 30(a) represents the DCTS signal with $e_{ref} = 0$ s⁻¹. In this case, only one peak is detected, and the peak discharge time and peak value are 22.5 s and 3.47×10^{12} cm⁻², respectively. From Eqs. (134) and (135), NS_{T1} and e_{T1} are determined to be 3.47×10^{12} cm⁻² and 4.44×10^{-2} s⁻¹, respectively. These obtained values are only a little different from NS_{T1} and e_{T1} using which the transient discharge current was simulated. In the figure, the broken and dashed-dotted lines, which correspond to Trap1 and Trap2 respectively, are simulated using the following equation;

$$NS_{Ti} e_{Ti} t \exp [-(e_{Ti} + e_{ref}) t + 1]. \quad (144)$$

Since it is found that Trap1 mainly affects the DCTS signal with $e_{ref} = 0$ s⁻¹, it is reasonable that the values determined using the maximum of the DCTS signal are close to NS_{T1} and e_{T1} , respectively.

The solid line in Fig. 30(b) represents the DCTS signal with $e_{ref} = -0.0089$ s⁻¹. In this case, two peaks appear. One peak value is 4.35×10^{12} cm⁻² at 29.4 s, and the

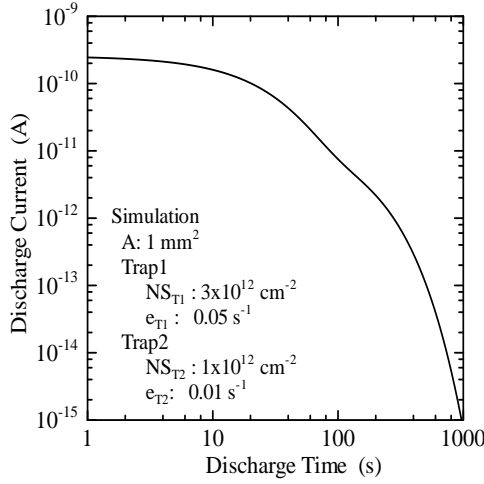


Figure 29. Transient discharge current simulated assuming two kinds of traps.

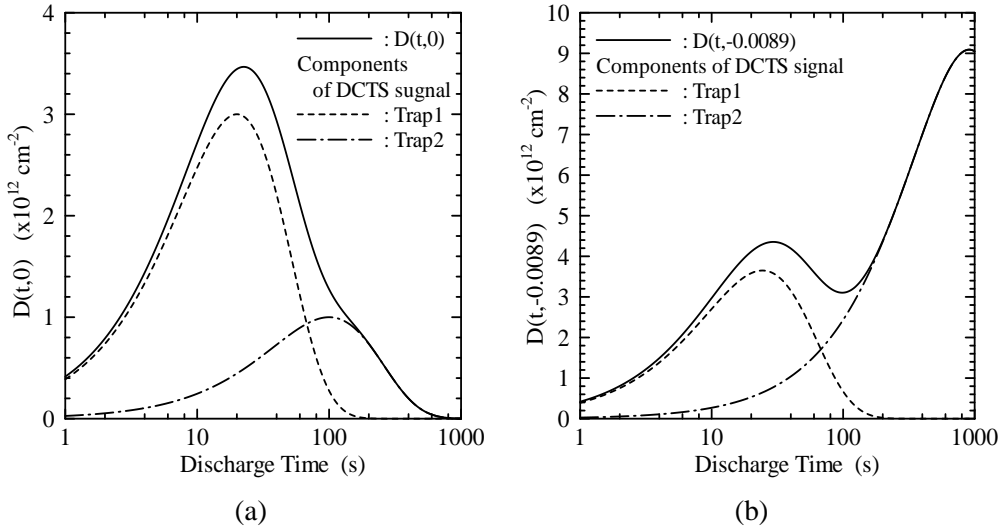


Figure 30. DCTS signals with (a) $e_{\text{ref}} = 0 \text{ s}^{-1}$ (solid line) and (b) $e_{\text{ref}} = 0.0089 \text{ s}^{-1}$ (solid line). The broken and dashed-dotted lines are simulated using Eq. (144) for Trap1 and Trap2, respectively.

other peak value is $9.09 \times 10^{12} \text{ cm}^{-2}$ at 910 s. From Eqs. (134) and (135), NS_{T1} and e_{T1} are determined to be $3.45 \times 10^{12} \text{ cm}^{-2}$ and $4.29 \times 10^{-2} \text{ s}^{-1}$, respectively, while NS_{T2} and e_{T2} are determined to be $9.99 \times 10^{11} \text{ cm}^{-2}$ and $1.00 \times 10^{-2} \text{ s}^{-1}$, respectively. In the figure, the broken and dashed-dotted lines, which are simulated using Eq. (144), correspond to Trap1 and Trap2, respectively. The peak corresponding to Trap2 is maximum when $e_{\text{ref}} = -0.0089 \text{ s}^{-1}$, although the peak corresponding to Trap1 is maximum when $e_{\text{ref}} = 0 \text{ s}^{-1}$. Therefore, it is natural that the values determined using the maximum of the

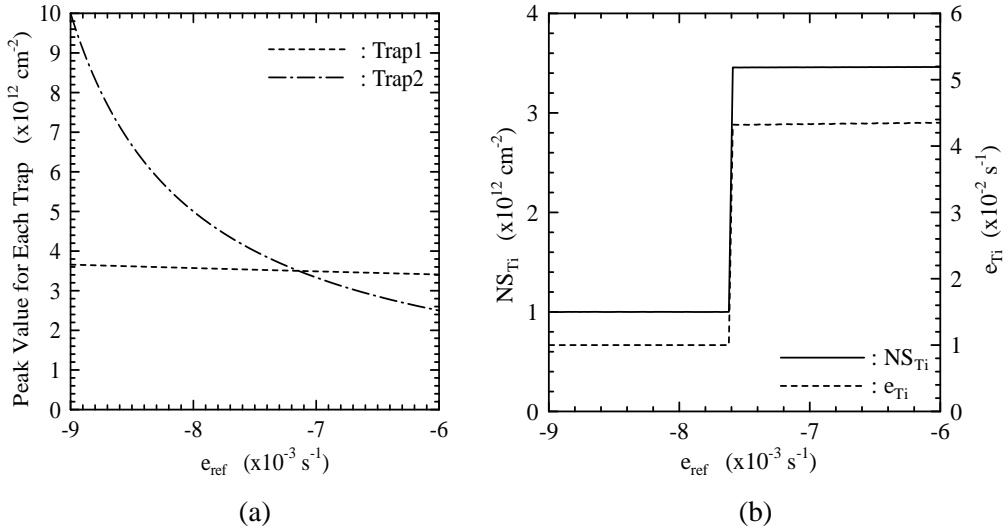


Figure 31. e_{ref} dependence of (a) peak value for Trap1 (broken line) or Trap2 (dashed-dotted line) and (b) NS_{Ti} or e_{Ti} determined from the maximum of the DCTS signal.

DCTS signal with $e_{\text{ref}} = -0.0089 \text{ s}^{-1}$ are close to NS_{T2} and e_{T2} , respectively.

Figure 31(a) shows the e_{ref} dependence of the peak value for Trap1 (broken line) or Trap2 (dashed-dotted line). The peak corresponding to Trap1 is maximum when $e_{\text{ref}} > -0.0071 \text{ s}^{-1}$, while the peak corresponding to Trap2 is maximum when $e_{\text{ref}} < -0.0071 \text{ s}^{-1}$. This suggests that it is possible to distinguish between two traps using the e_{ref} dependence of NS_T or e_T determined using the maximum of the DCTS signal.

Figure 31(b) shows the e_{ref} dependence of NS_T or e_T determined from the maximum of the DCTS signal. The two discrete values of e_T or NS_T clearly appear in the figure. Moreover, the obtained values are close to the values using which the transient discharge current was simulated. Therefore, it is found that DCTS can distinguish among traps with close emission rates by changing e_{ref} .

7.5. DCTS for Semi-insulating Semiconductors

After native oxide layers on a 0.37-mm-thick high-purity semi-insulating on-axis 4H-SiC wafer were removed using HF, Ni electrodes with a radius of 1.25 mm were evaporated in vacuum onto both sides of the samples [47, 48]. Figure 32(a) shows the transient reverse current $I_{\text{dis}}(t)$ at 303 K after a V_{dis} of -100 V is applied to a diode held at thermal equilibrium ($V_{\text{cha}} = 0 \text{ V}$) for 5 min. In the figure, \bigcirc represents the experimental $I_{\text{dis}}(t)$, and the solid line is calculated by interpolating the experimental $I_{\text{dis}}(t)$ with a cubic smoothing natural spline function.

Figure 32(b) shows $D(t, e_{\text{ref}})$ calculated with an e_{ref} of 0 s^{-1} using Eq. (136). There are two peaks labeled Peak1 and Peak2, and the corresponding traps are here referred to as SI1 and SI2, respectively. From t_{Peak1} and $D(t_{\text{Peak1}}, 0)$, the values of NS_{T1} and e_{T1} for SI1 were determined to be $1.6 \times 10^{11} \text{ cm}^{-2}$ and $5.5 \times 10^{-2} \text{ s}^{-1}$, respectively, while from

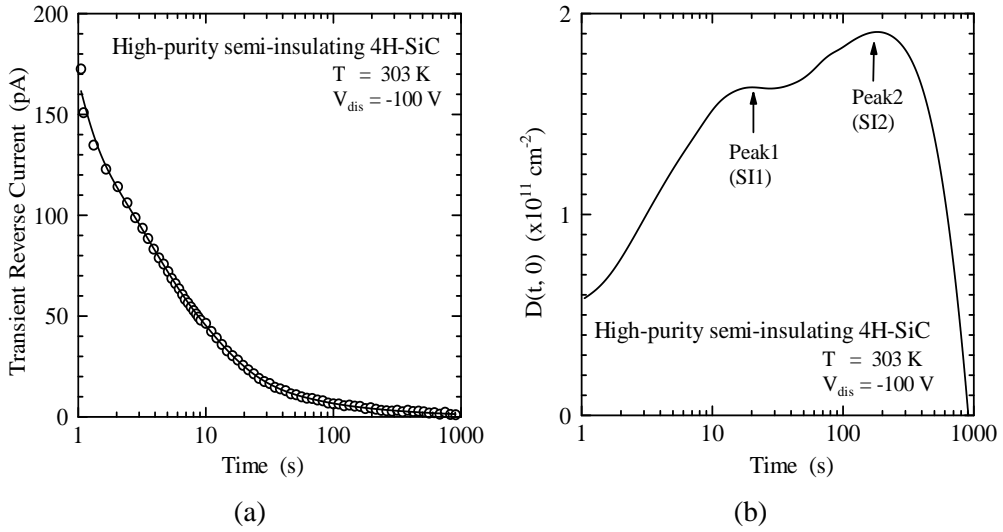


Figure 32. Characteristics of Schottky barrier diode with high-purity semi-insulating 4H-SiC at 303 K; (a) transient reverse current and (b) DCTS signal.

Table 6. Energy levels and cross sections of traps in high-purity semi-insulating 4H-SiC determined by DCTS.

Trap species	Energy level (eV)	Cross section (cm ²)
SI1	0.78	2×10^{-15}
SI2	0.85	2×10^{-15}
SI3	0.90	1×10^{-13}
SI4	1.2	8×10^{-12}
SI5	1.4	9×10^{-10}

t_{Peak2} and $D(t_{\text{Peak2}}, 0)$, NS_{T2} and e_{T2} for SI2 were determined to be $1.9 \times 10^{11} \text{ cm}^{-2}$ and $5.5 \times 10^{-3} \text{ s}^{-1}$, respectively.

Finally, five types of traps could be observed in the temperature range between 283 and 373 K. Figure 33 shows the relationship between e_{Ti}/T^2 and $1/T$ for five different traps. The optimum straight line fitting to experimental data for each trap could be obtained, from which E_{Ti} and σ_{Ti} could be determined using Eqs. (105)-(108), and listed in Table 6.

7.6. DCTS for Crystalline Insulators

Pb(Zr,Ti)O₃ (PZT) thin films were deposited on Pt/SiO₂/(100)Si substrates at 570 °C by metalorganic chemical vapor deposition, using Pb(C₂H₅)₄, Zr(O-t-C₄H₉)₄ and Ti(O-i-C₃H₇)₄ as source precursors [46]. The thickness of the PZT films was 200 nm. The area of the Pt top electrode was 0.79 mm². DCTS measurements of Pt/PZT/Pt capacitors were performed at 373 K in an oxidation atmosphere (Ar : O₂ = 1 : 1 at 1 atom). The transient

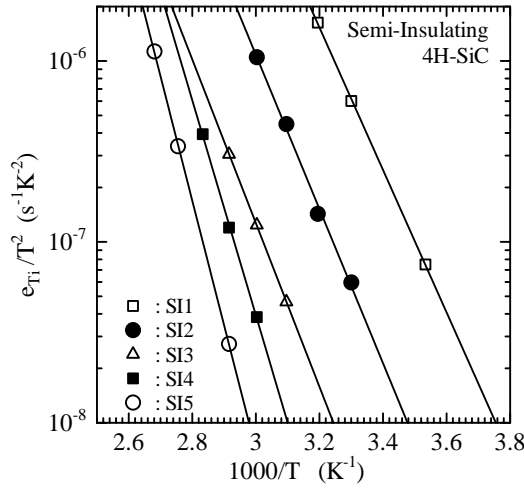


Figure 33. Relationship between $e_{Ti}/T^2 - 1/T$.

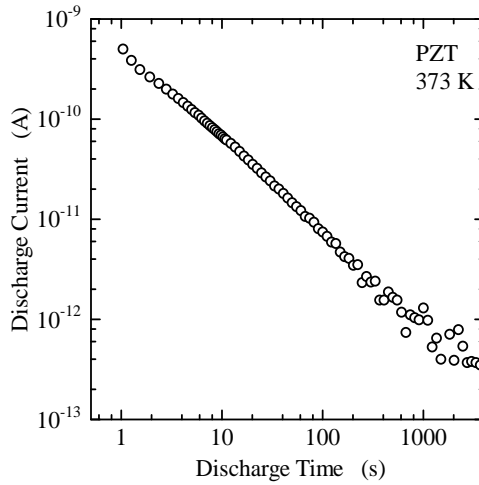


Figure 34. Transient discharge current in Pt/PZT/Pt capacitor.

discharge current was measured at $V_{dis} = 0$ V, after V_{cha} of 2 V was applied to the capacitor in the interval of 600 s. Figure 34 shows $I_{dis}(t)$ in the Pt/PZT/Pt capacitor. To search a peak of the DCTS signal precisely, the DCTS signal was calculated by interpolating $I_{dis}(t)$ with a cubic smoothing natural spline function.

The solid line in Fig. 35(a) represents the DCTS signal with $e_{ref} = 0$ s $^{-1}$. The maximum discharge time and maximum value were 4.09 s and 1.54×10^{12} cm $^{-2}$, respectively. From Eqs. (134) and (135), NS_T and e_T were determined to be 1.54×10^{12} cm $^{-2}$ and 2.44×10^{-2} s $^{-1}$, respectively. In the case that the traps are uniformly distributed in the film, the trap density is estimated to be 7.70×10^{16} cm $^{-3}$, because the film thickness was 200 nm. The broken line represents the signal simulated using Eq. (144) with the ob-

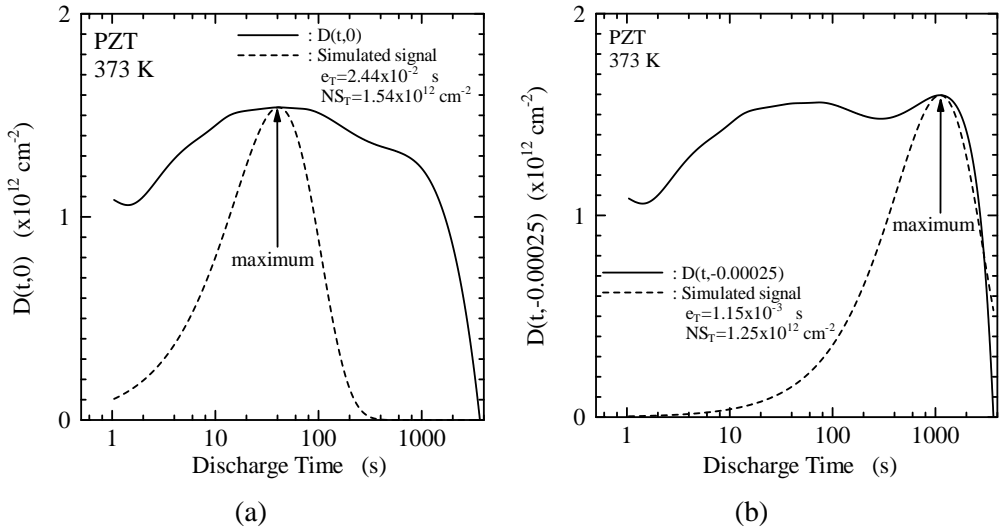


Figure 35. DCTS signal (solid line) with (a) $e_{\text{ref}} = 0 \text{ s}^{-1}$ and (b) $e_{\text{ref}} = -0.00025 \text{ s}^{-1}$, which is calculated by interpolating $I_{\text{dis}}(t)$ with a cubic smoothing natural spline function. The broken line corresponds to the signal simulated using Eq. (144) with NS_{T} and e_{T} determined from the maximum of the DCTS signal.

tained values. Since the solid line is much broader than the broken line, the DCTS signal is considered to be affected by several traps with close emission rates.

The solid line in Fig. 35(b) represents the DCTS signal with $e_{\text{ref}} = -0.00025 \text{ s}^{-1}$. The maximum discharge time and maximum value were 1111 s and $1.60 \times 10^{12} \text{ cm}^{-2}$, respectively. From Eqs. (134) and (135), NS_{T} and e_{T} were determined to be $1.25 \times 10^{12} \text{ cm}^{-2}$ and $1.15 \times 10^{-2} \text{ s}^{-1}$, respectively.

The broken line represents the signal simulated using Eq. (144) with the obtained values. Since NS_{T} and e_{T} for $e_{\text{ref}} = -0.00025 \text{ s}^{-1}$ are different from those for $e_{\text{ref}} = 0 \text{ s}^{-1}$, at least two kinds of traps with close emission rates are included in the PZT film.

Figure 36(a) shows the e_{ref} dependence of NS_{T} (solid line) or e_{T} (broken line) determined from the maximum of the DCTS signal at $e_{\text{ref}} < 0$. Three discrete values of e_{T} or NS_{T} clearly appear in the figure. Moreover, the e_{ref} range of the constant NS_{T} clearly corresponds one-to-one to the e_{ref} range of the constant e_{T} . Therefore, it is found that DCTS can distinguish among three kinds of traps (Trap1, Trap2, and Trap3) with close emission rates by changing negative e_{ref} . From Fig. 36(a), NS_{T} and e_{T} of each trap can be determined; $e_{\text{T}1}$ and $NS_{\text{T}1}$ are $1.15 \times 10^{-3} \text{ s}^{-1}$ and $1.2 \times 10^{12} \text{ cm}^{-2}$, respectively, and $e_{\text{T}2}$ and $NS_{\text{T}2}$ are $1.39 \times 10^{-2} \text{ s}^{-1}$ and $1.53 \times 10^{12} \text{ cm}^{-2}$, respectively, and $e_{\text{T}3}$ and $NS_{\text{T}3}$ are $2.3 \times 10^{-2} \text{ s}^{-1}$ and $1.54 \times 10^{12} \text{ cm}^{-2}$, respectively.

Figure 36(b) shows the e_{ref} dependence of NS_{T} (solid line) or e_{T} (broken line) determined from the maximum of the DCTS signal at $e_{\text{ref}} \geq 0$. In addition to the three kinds of traps determined in Fig. 36(a), another two kinds of traps (Trap4 and Trap5) are considered to be included in this thin film. $e_{\text{T}4}$ and $NS_{\text{T}4}$ are approximately $7 \times 10^{-2} \text{ s}^{-1}$ and $1.5 \times 10^{12} \text{ cm}^{-2}$, respectively. On the other hand, the emission rate of Trap5 may be

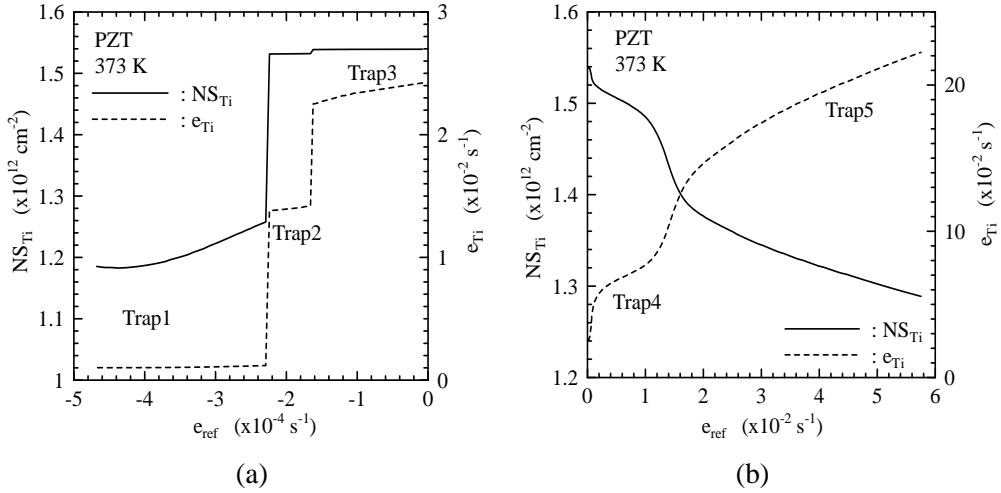


Figure 36. e_{ref} dependence of NS_{Ti} (solid line) or e_{Ti} (broken line) determined from the maximum of the DCTS signal at (a) $e_{ref} < 0$ and (b) $e_{ref} \geq 0$.

fluctuated, because both e_T and NS_T of Trap5 change gradually with e_{ref} in the figure.

7.7. DCTS for Amorphous Insulators

76 nm-thick SiN_x films were deposited on heavily-doped p-type c-Si (p^+ c-Si) at a substrate temperature of 500 °C by direct photo-chemical vapor deposition with a low-pressure mercury lamp using N_2 -diluted mixtures of SiH_4 and NH_3 [44, 45]. An Al electrode with 3.14 mm^2 was deposited on SiN_x by vacuum evaporation. Here, p^+ c-Si and Al act as electrodes of a capacitor.

Figure 37(a) shows the I - V characteristics for Capacitors A and B. The leakage current for Capacitor B at low applied biases (< 35 V) was higher than that for Capacitor A. To investigate the reason, $I_{dis}(t)$ for Capacitors A and B were measured. During the charging time (i.e., in $-600 \text{ s} < t < 0 \text{ s}$), V_{cha} of 50 V was applied to the Al electrode of an Al/ SiN_x / p^+ c-Si capacitor. Applying a positive voltage to the Al electrode implies that holes injected from the Al electrode should flow through SiN_x . $I_{dis}(t)$ was measured at $V_{dis} = 0$ in $t > 0 \text{ s}$. Figure 37(b) presents the data of $D(t)$ for Capacitors A and B. $D(t)$ was calculated from the measured $I_{dis}(t)$ using Eq. (136) with $e_{ref} = 0 \text{ s}^{-1}$, that is, $D(t) = D(t, 0)$.

When trap levels in the film are continuously distributed in the band gap, Eq. (130) is rewritten as

$$g[E(t)] \cong \frac{D(t) \exp(-1)}{kTL} \quad (145)$$

and

$$E(t) - E_V = kT \ln(\nu_h t), \quad (146)$$

which are similar to Eqs. (128) and (129). Here, L is the thickness (76 nm) of SiN_x . The $g(E)$ above E_V was calculated from Eqs. (145) and (146) and shown in Fig. 37(b), where

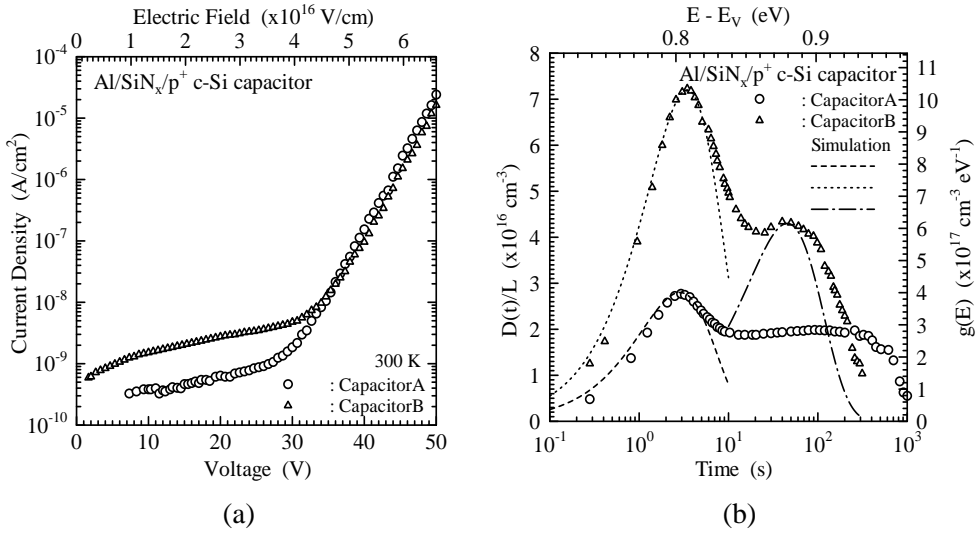


Figure 37. I - V characteristics (a) and DCTS signals (b) for Capacitors A and B. Here, L is 7.6×10^{-6} cm.

it was assumed that $\nu_h = 10^{13} s^{-1}$ because ν_h is related to an optical phonon frequency in the film and is equal to or less than the order of $10^{13} s^{-1}$. As is clear from Fig.37, the leakage current at < 35 V is correlated with the $g(E)$.

The peak value (NS_{T1}/L) and time (e_{T1}) of $D(t)$ for Capacitor A were $2.8 \times 10^{16} cm^{-3}$ and $e_{T1} = 0.35 s^{-1}$, respectively. Assuming that this peak is due to a discrete trap, the component of $D(t)$ corresponding to this peak is calculated using Eq. (144) and shown in the broken line of Fig. 37(b), which is in good agreement with \bigcirc . Therefore, one discrete trap with $E_V - E$ of ~ 0.81 eV and traps energetically-distributed between 0.85 and 0.96 eV exist in Capacitor A.

From peaks of ($NS_{T1}/L = 7.2 \times 10^{16} cm^{-3}$ and $e_{T1} = 0.29 s^{-1}$) and ($NS_{T2}/L = 4.3 \times 10^{16} cm^{-3}$ and $e_{T2} = 0.022 s^{-1}$) for Capacitor B, on the other hand, the corresponding components represent the dotted and dashed-dotted lines in Fig. 37(b), which are in good agreement with \triangle at $10^{-1} - 10$ s and $10 - 10^2$ s, respectively. In the SiN_x film of Capacitor B, therefore, two discrete traps with approximately 0.81 and 0.88 eV were included.

8. Conclusion

Several methods to determine densities and energy levels of impurities and defects affecting the majority-carrier concentration in semiconductors whose resistivities vary from low to extremely high have been discussed;

1. Free carrier Concentration Spectroscopy (FCCS) determining densities and energy levels in a semiconductor using the temperature dependence of the majority-carrier concentration without any assumptions regarding impurities and defects,
2. Heterojunction-Monitored Capacitance Spectroscopy (HMCS) determining the

density-of-states in high-resistivity amorphous semiconductors using the transient capacitance of an amorphous/crystalline semiconductor heterojunction,

3. Discharge Current Transient Spectroscopy (DCTS) determining densities and energy levels in a semi-insulating semiconductor or an insulator using the transient current of a diode.

On the other hand, the influence of the excited states of dopants with deep energy levels on the majority-carrier concentration have been discussed, and a unique distribution function for dopants including the effect of the excited states of dopants has been proposed and experimentally tested.

References

- [1] Lang, D. V. *J. Appl. Phys.* 1974, vol. 45, 3023-3032.
- [2] Danno, K.; Kimoto, T. *Jpn. J. Appl. Phys.* 2006, vol. 45, L285-L287.
- [3] Danno, K.; Kimoto, T. *Mater. Sci. Forum* 2007, vol. 556-557, 331-334.
- [4] Haering, R. R.; Adams, E. N. *Phys. Rev.* 1960, vol. 117, 451-454.
- [5] Sze, S. M. *Physics of Semiconductor Devices* 2nd ed.; Wiley: New York, 1981, chapter 1.
- [6] Hoffmann, H. J. *Appl. Phys.* 1979, vol. 19, 307-312.
- [7] Hoffmann, H. J.; Nakayama, H.; Nishino, T.; Hamakawa, H. *Appl. Phys. A: Mater. Sci. & Processing* 1984, vol. 33, 47-50.
- [8] Okushi, H. *Philos. Mag. B* 1985, vol. 52, 33-57.
- [9] Matsuura, H.; Sonoi, K. *Jpn. J. Appl. Phys.* 1996, vol. 35, L555-L557.
- [10] Matsuura, H. *Jpn. J. Appl. Phys.* 1997, vol. 36, 3541-3547.
- [11] Matsuura, H.; Masuda, Y.; Chen, Y.; Nishino, S. *Jpn. J. Appl. Phys.* 2000, vol. 39, 5069-5075.
- [12] Suzuki, A.; Uemoto, A.; Shigeta, M.; Furukawa, K.; Nakajima, S. *Appl. Phys. Lett.* 1986, vol. 49, 450-452.
- [13] Freitas, Jr., J. A.; Bishop, S. G.; Nordquist, Jr., P. E. R.; Gipe, M. L. *Appl. Phys. Lett.* 1988, vol. 52, 1695-1697.
- [14] Kaplan, R.; Wagner, R. J.; Kim, H. J.; Davis, R. F. *Solid State Commun.* 1985, vol. 55, 67-69.
- [15] Ikeda, M.; Matsunami, H.; Tanaka, T. *Phys. Rev. B* 1980, vol. 22, 2842-2854.

-
- [16] Götz, W.; Schöner, A.; Pensl, G.; Suttrop, W.; Choyke, W. J.; Stein, R.; Leibenzeder, S. *J. Appl. Phys.* 1993, vol. 73, 3332-3338.
- [17] Matsuura, H.; Morita, K.; Nishikawa, K.; Mizukoshi, T.; Segawa, M.; Susaki, W. *Jpn. J. Appl. Phys.* 2002, vol. 41, 496-500.
- [18] Matsuura, H.; Nishikawa, K.; Segawa, M.; Susaki, W. *Jpn. J. Appl. Phys.* 2006, vol. 45, 6373-6375.
- [19] Matsuura, H.; Nishikawa, K. *J. Appl. Phys.* 2005, vol. 97, 093711 1-7.
- [20] Matsuura, H.; Nagasawa, H.; Yagi, K.; Kawahara, T. *J. Appl. Phys.* 2004, vol. 96, 7346-7351.
- [21] Kagamihara, S.; Matsuura, H.; Hatakeyama, T.; Watanabe, T.; Kushibe, M.; Shinohe, T.; Arai, K. *J. Appl. Phys.* 2004, vol. 96, 5601-5606.
- [22] Matsuura, H.; Komeda, M.; Kagamihara, S.; Iwata, H.; Ishihara, R.; Hatakeyama, T.; Watanabe, T.; Kojima, K.; Shinohe, T.; Arai, K. *J. Appl. Phys.* 2004, vol. 96, 2708-2715.
- [23] Matsuura, H.; Kagamihara, S.; Itoh, Y.; Ohshima, T.; Itoh, H. *Physica B* 2006, vol. 376-377, 342-345.
- [24] Matsuura, H.; Minohara, N.; Ohshima, T. *J. Appl. Phys.* 2008, vol. 104, 043702 1-6.
- [25] Matsuura, H.; Iwata, H.; Kagamihara, S.; Ishihara, R.; Komeda, M.; Imai, H.; Kikuta, M.; Inoue, Y.; Hisamatsu, T.; Kawakita, S.; Ohshima, T.; Itoh, H. *Jpn. J. Appl. Phys.* 2006, vol. 45, 2648-2655.
- [26] Yu, P. Y.; Cardona, M. *Fundamentals of Semiconductors: Physics and Materials Properties* 2nd ed.; Springer, Berlin, 1999; pp. 156 and 160.
- [27] Sapoval B.; Hermann, C. *Physics of Semiconductors*; Springer-Verlag, New York, 1993; pp. 73 and 112.
- [28] Singh, J. *Semiconductor Devices: An Introduction*; McGraw-Hill, New York, 1994; p. 110.
- [29] Smith, R. A. *Semiconductors* 2nd ed.; Cambridge University Press, Cambridge 1978; p. 92.
- [30] Brennan, K. F. *The Physics of Semiconductors with Applications to Optoelectronic Devices*; Cambridge University Press, Cambridge, 1999; p. 292.
- [31] Ashcroft N. W.; Mermin, N. D. *Solid State Physics*; Holt Rinehart and Winston, Philadelphia, 1976; pp. 581 and 586.
- [32] Troffer, T.; Schadt, M.; Frank, T.; Itoh, H.; Pensl, G.; Heindl, J.; Strunk, H. P.; Maier, M. *Phys. Status Solidi A* 1997, vol. 162, 277-298.

-
- [33] Schulze, N.; Gajowski, J.; Semmelroth, K.; Laube, M.; Pensl, G. *Mater. Sci. Forum* 2001, vol. 353-356, 45-48.
- [34] Matsuura, H. *New J. Phys.* 2002, vol. 4, 12.1-12.15 [<http://www.njp.org/>].
- [35] Matsuura, H. *J. Appl. Phys.* 2004, vol. 95, 4213-.
- [36] Heer, C. V. *Statistical Mechanics, Kinetic Theory, and Stochastic Processes*; Academic Press, New York, 1972; p. 224.
- [37] Matsuura, H.; Yanase, H.; Takahashi, M. *Jpn. J. Appl. Phys.* 2008, vol. 47, 7052-7055.
- [38] Matsuura, H.; Okuno, T.; Okushi, H.; Tanaka, K. *J. Appl. Phys.* 1984, vol. 55, 1012-1019.
- [39] Matsuura, H. *J. Appl. Phys.* 1988, vol. 64. 1964-1973.
- [40] Matsuura, H. *Jpn. J. Appl. Phys.* 1988, vol. 27, L513-L515.
- [41] Matsuura, H. *Jpn. J. Appl. Phys.* 1988, vol. 27, L516-L518.
- [42] Matsuura H.; Okushi, H. In *Amorphous and Microcrystalline Semiconductor Devices II: Materials and Device Physics*; Kanicki, J.; Ed.; Artech House, Boston, 1992; chapter 11.
- [43] Matsuura, H.; Okuno, T.; Okushi, H.; Yamasaki, S.; Matsuda, A.; Hata, N.; Oheda, H.; Tanaka, K. *Jpn. J. Appl. Phys.* 1983, vol. 22, L197-L199.
- [44] Matsuura, H.; Yoshimoto, M.; Matsunami, H. *Jpn. J. Appl. Phys.* 1995, vol. 34, L185-L187.
- [45] Matsuura, H.; Yoshimoto, M.; Matsunami, H. *Jpn. J. Appl. Phys.* 1995, vol. 34, L371-L374.
- [46] Matsuura, H.; Hase, T.; Sekimoto, Y.; Uchida, M.; Simizu, M. *J. Appl. Phys.* 2002, vol. 91, 2085-2092.
- [47] Matsuura, H.; Kagawa, Y.; Takahashi, M.; Tano, S.; Miyake, T. *Jpn. J. Appl. Phys.* 2009, vol. 48, 056504 1-4.
- [48] Matsuura, H.; Takahashi, M.; Kagawa, Y.; Tano, S.; Miyake, T. *Mater. Sci. Forum* 2009, vol. 615-617, 385-388.